Schweizerische Eidgenossenschaft
Confédération suisse
Confederazione Svizzera
Confederaziun svizra

Federal Department of the Environment, Transport, Energy and Communications DETEC

Swiss Federal Office of Energy SFOE
Energy Research and Cleantech Division

HIRES

High-resolution CFD grade Experiments for low-Pr number flows in Fuel Assemblies of liquid metal cooled Reactors

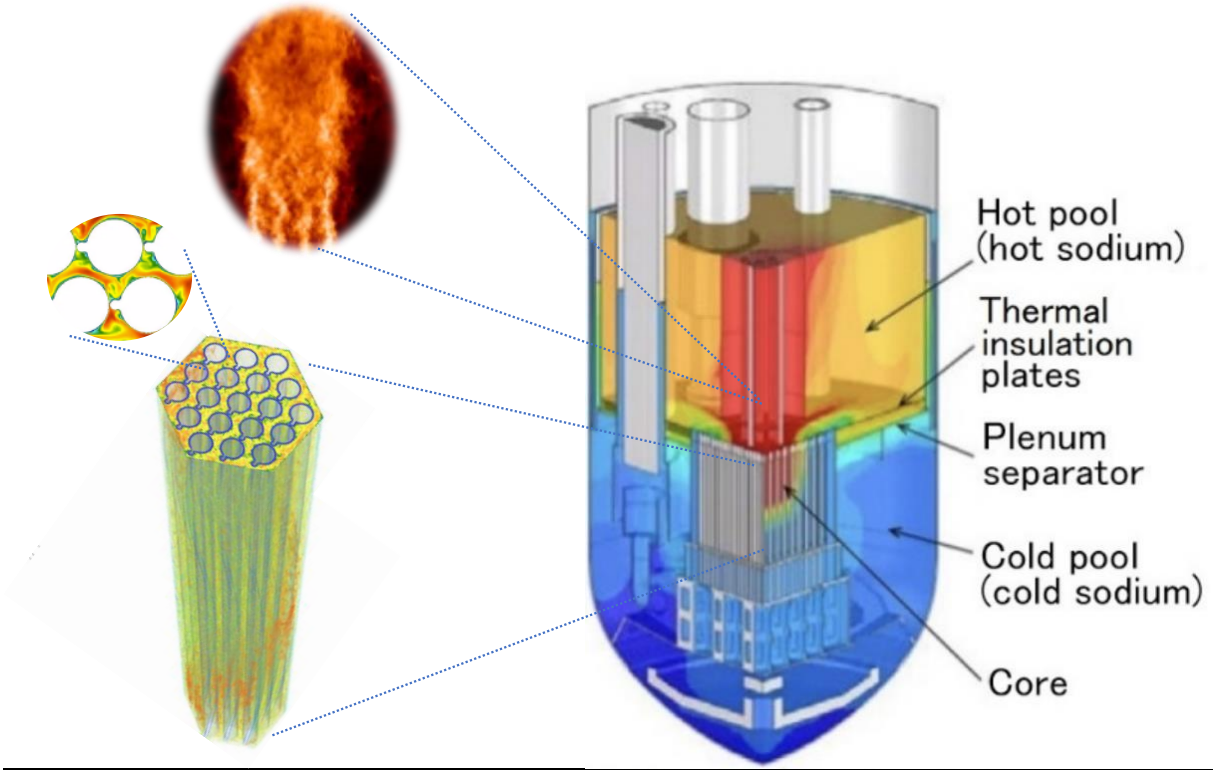

Source: see reference section

Date: 8/11/2024

Location: Bern

Publisher:
Swiss Federal Office of Energy SFOE
Energy Research and Cleantech
CH-3003 Bern
www.bfe.admin.ch

Co-financing:
ETHZ
Sonneggstrasse 3, 8092 Zürich
www.ethz.ch

Subsidy recipients:
ETHZ
Sonneggstrasse 3, 8092 Zürich
www.ethz.ch

Authors:
Annalisa Manera, ETH-Zurich
Victor Petrov, Paul Scherrer Institut
Valentina Valori, ETH-Zurich
Sergii Nichenko, ETH-Zurich
Taehwan Ahn, ETH-Zurich
Axel Monney, ETH-Zurich
William Bissels, Paul Scherrer Institut,

SFOE project coordinators:
Michael Moser, michael.moser@bfe.admin.ch

SFOE contract number: SI/502338-01

Summary

The HIRES project aims at filling the gap of high resolution data needs on mixing and velocity field in geometries and conditions relevant for liquid-metal-cooled fast reactors. The ultimate goal is to use the data to validate computational fluid dynamics models, so that they can be used to to assess designs of liquid-metal-cooled fast reactors.

Three experimental setups have been designed and built:

- the first facility was aimed at the investigation of mixing of buoyant jets in the presence of uniform and stratified environments, of relevance for pool-type liquid metal fast reactors. This task required the development of a novel analytical models to predict refractive indices of fluid mixtures, so that high-resolution optical measurement techniques could be applied in the presence of density differences;
- the second facility was focused on the investigation of the occurrence of fuel cladding hot spots caused by the presence of wire-wrap, typical of liquid-metal-cooled fuel assemblies designs. The conditions at which hot spots can occur were identified. The experimental data have been used to validate computational models. Those, in combination with the experimental data, have been used to define optimal wire-wrap geometries to mitigate the occurrence of hot spots.
- finally, a third experimental facility was designed to investigate the potential occurrence of fuel pins failure cascades in lead cooled fast reactors. It was found that the release of fission gas from a failed pin poses the greatest risk to adjacent fuel pins. In particular, high-speed imaging has revealed that bubble growth initially localized to a single spot, has the potential to surround adjacent fuel pins, leading to potential pins failure propagation.

Contents

Abbreviations

CCFL	Counter-current flow limitation
CFD	Computational fluid-dynamics
IR	Infra-red
LFR	Lead fast reactor
LMFR	Liquid metal cooled fast reactor
PHRS	Passive Heat Removal System
PIV	Particle image velocimetry
PLIF	Planar laser-induced fluorescence
PTV	Particle Tracking Velocimetry
PMMA	Polymer of methyl methacrylate
RAM	Random access memory
RANS	Reynolds-Averaged Navier-Stokes
RCP	Reactor coolant pumps
RIM	Refractive index matching
SBO	Station black out
SFR	Sodium fast Reactor
SS	stainless steel
UNIFAC	UNIQUAC Functional-group Activity Coefficients
UNIQUAC	Universal quasi-chemical

1 Introduction

1.1 Background

The project is focused on liquid-metal-cooled fast reactors. Such reactors are of strong interest because they would allow a much more efficient use of nuclear fuel compared to light water reactors (LWRs). More specifically, fast reactors can extract about 60 times more energy per unit of uranium than a thermal reactor [IAEA, 2012]. As they can produce more energy from the same amount of fuel, the deployment of such type of reactors would also result in a considerable reduction of the amounts of nuclear waste produced. Right now Russia is operating the BN-600 and BN-800 sodium-cooled reactors, and is building the lead-cooled BREST reactor. In the USA, Terrapower has brought a sodium-cooled reactor on the market with its first unit planned for construction in Wyoming (a construction license for the Wyoming site has been submitted to the US Nuclear Regulatory Commission in 2024), while Westinghouse is working at the design of a lead-cooled fast reactor. China is building two sodium-cooled reactors (CFR-600), with the first unit in operation since 2023 and the second unit expected to become operational in 2026. Lastly, India has completed a 500 MWe sodium-cooled reactor, which is expected to start operation in 2025.

Liquid metal coolants combine large thermal conductivities with large thermal capacities and low viscosities, which make them very attractive as coolants for high power density applications such as sodium-cooled fast-spectrum nuclear reactors. As a consequence of their low Prandtl number, the traditional eddy viscosity approach to turbulent heat transport begins to break down for liquid metals; there is a mismatch between the length and time scales associated with thermal and viscous boundary layer. Advances in CFD-based predictive modelling of thermal hydraulic performance of advanced reactors using these coolants has been hindered by the lack of sufficiently high-resolution measurements. The goal of the present project is to close identified experimental gaps by providing a comprehensive set of carefully coordinated separate effects experiments.

In particular, phenomena of interest are: the mixing of buoyant jets and their stability in uniform and stratified environments, of relevance for pool-type liquid metal fast reactors (LMFR); the occurrence of hot spots in fuel pins cladding caused by the presence of the wire-wrap used in LMFR to prevent contact between neighboring fuel pins; the potential occurrence of fuel pins failure cascades in the case in which a fuel pin in a LMFR core cracks with a subsequent ejection of fission products. In this case, the resulting fission products gas bubble could engulf neighboring pins, significantly deteriorating heat transfer, leading to potential failure of these neighboring pins.

1.2 Project objectives

The objective of the HIRES project is to close existing gaps in high-resolution data that are needed to validate computational fluid dynamic models (CFD) for mixing and heat transfer in liquid metal flows. The ultimate goal is to validate CFD models to be used for the assessment of safety and operational margin of liquid-metal-cooled fast reactors.

More specifically, three separate experimental setups have been designed, built and equipped with advanced, high-resolution instrumentation. Goal of the three experimental facilities is to address, respectively:

a. the mixing of buoyant jets in uniform and stratified environments, relevant for the stratification in the LMFR pool upper plenum and for the occurrence of thermal striping of the upper plenum internals structures (details are presented in chapter 2);

b. the occurrence of hot spots on fuel cladding in the presence of wire-wrap, typical of LMFR fuel assemblies designs (details are presented in chapter 3);

c. the occurrence of fuel pin cascade failure due to the effect of fission gas release on the heat removal of neighbouring fuel pins (details are presented in chapter 4).

Figure 1 illustrates the areas addressed by the experimental campaigns (a) to (c).

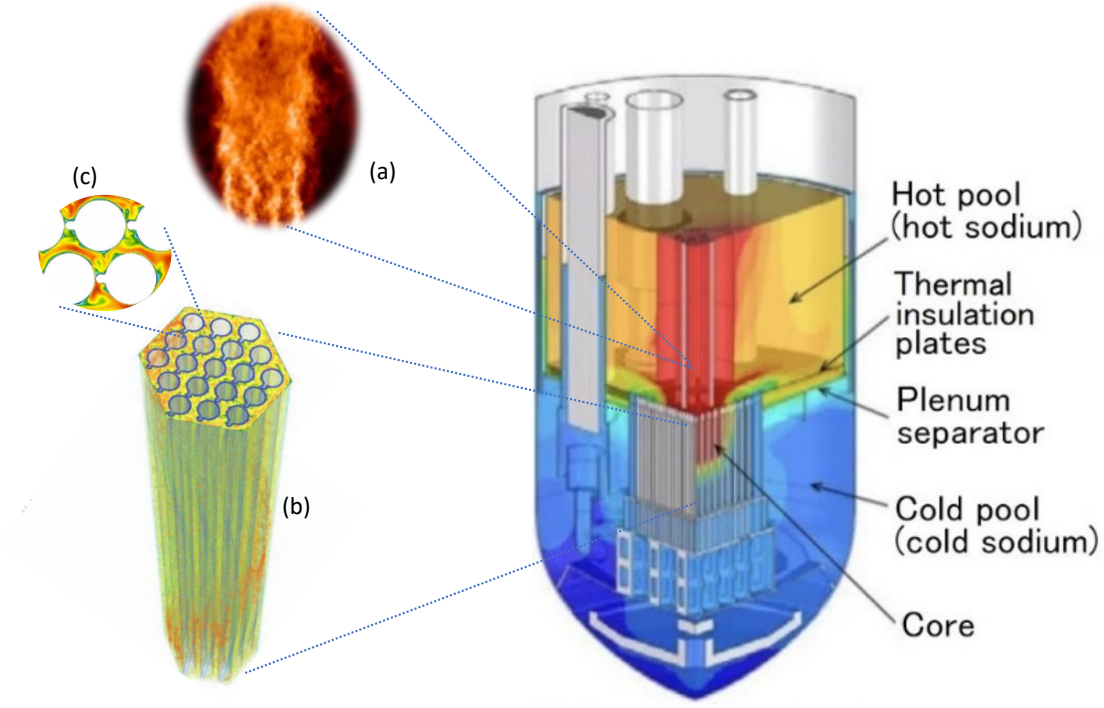

Figure 1: Illustration of a sodium-cooled fast reactor and the three area (a) – (c) addressed by the proposed experimental campaigns.

2 Task 1: mixing of buoyant jets in uniform and stratified environments

Mixing in large enclosures and thermal stratification play an important role in liquid metal cooled reactors. Both SFR pool reactor designs, as well as the Westinghouse LFR feature a hot pool where liquid metal (sodium or lead), after raising from the core, moves radially into heat exchangers and is then drawn by the RCPs located downstream of the heat exchangers (see Figure 1).

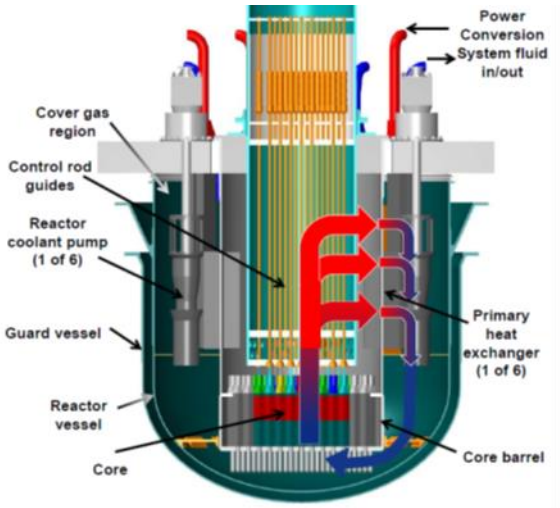

Figure 2: Cross section of reactor coolant system of the Westinghouse LFR

During safety events such as Station Blackout (SBO) the RCPs coast down and the primary heat exchangers are no longer effective in removing heat. In this scenario decay heat removal relies on the Passive Heat Removal System (PHRS), which removes heat by natural convection. The PHRS is always on, even during normal reactor operation and shutdown, thus resulting in continuous thermal losses. In these operational modes (e.g. normal operation or shutdown), however, the temperature of the reactor vessel is not sufficient to promote significant radiative heat transfer, thus limiting these radiative losses to low values. Instead, when the lead pool temperature increases as a result of an accident, PHRS starts to remove more and more heat, thus increasing its effectiveness just when it is needed. In this operating regime, natural circulation occurs within the vessel, with hot lead raising from the core and with hot lead raising from the core and being subsequentially cooled while flowing downward along the RV wall, due to PHRS operation. Thermal stratification, especially in the hot pool but also in some regions of the cold pool, may hinder effective natural circulation thus lowering PHRS performance.

In LMFRs, core channels are typically hydro-dynamically isolated so that there exists a considerable temperature variation at the exit of adjacent fuel assemblies. The upper plenum region behaves then as a region of parallel flow jets originating from the fuel assemblies outlets (Shashikant et al., 2013). The mixing of the buoyant jets with the surrounding environment will also affect the thermal stratification in the liquid metal pool.

The behaviour of buoyant jets in stratified environments is challenging for current CFD RANS models, which are most widely used for nuclear safety relevant applications. In order to further develop and validate CFD RANS models, a database of well-controlled, high-resolution experiments are needed about the interaction of buoyant jets with stratified environments. Optical techniques such as PIV and PLIF are used to measure local velocity components fluctuations and their cross-correlations (e.g. Reynolds stresses). However, with buoyant jets, the presence of density difference result also in changes of the refractive index, which will blur and corrupt PIV and PLIF images. Refractive index matching (RIM) techniques have been applied since the 1970s to overcome this issue, however because of the empiricism in the identification of adequate fluids, density differences of up to about 3% were reported in the literature. A breakthrough was achieved by our research group in 2018 (Krohn et al., 2018) through the developed of a methodology, that allows to systematically identify the set of RIM fluids. The methodology was successfully applied to density differences of almost 9%, much larger than what achieved in the past 50 years. The developed methodology requires however to experimentally map the refractive index of several mixture concentrations.

In section 2.1 a summary is given about a theoretical model that has been developed and validated, which allows to significantly reduce the number of measurements needed to map the refractive index.

In section 2.2, the RIM technique is applied to build a high-resolution experimental database on buoyant jets in stratified environments that can be used to validate and further develop CFD models.

2.1 Refractive index matching technique

Predicting the thermophysical properties of liquid mixtures, such as density, refractive index, and viscosity, is crucial for various chemical engineering applications. Traditional methods for determining these properties often involve extensive experimental work, which can be costly and time-consuming. Theoretical models offer an alternative approach for predicting these properties, and several models have been developed, including the Tait-like equation, PC-SAFT, Peng-Robinson equations of state, and artificial neural networks.

This work focuses on the UNIFAC (UNIQUAC Functional-group Activity Coefficients) model, a group contribution method originally developed for estimating activity coefficients in non-ideal mixtures. By considering interactions between functional groups rather than entire molecules, UNIFAC simplifies the prediction of mixture behaviour and allows estimation of properties for a wide range of systems, even in the absence of experimental data. This work aims to expand the application of UNIFAC to predict physical properties of multicomponent systems, such as molar volumes (densities) and refractive index, by presenting an algorithm for calculating surface area fractions in mixed systems. This algorithm also reconstructs the structure of the liquid phase, providing insights into the structure of liquid phases of multicomponent systems. Preliminary calculations using this method have shown promising results, suggesting its potential for predicting a variety of properties in mixed systems. While the accuracy of such predictions may not always match experimental measurements, this method can serve as a source of estimated data to guide and plan experimental investigations, reducing the time needed to study complex multicomponent systems.

In the UNIFAC model, the liquid phase is characterized by local area fractions, which describe the distribution of different functional groups on the molecular surface (Fredenslund et al., 1975). The interactions between these groups are quantified by interaction parameters, which are derived from experimental data or quantum chemical calculations. These parameters are used to calculate the activity coefficients, which in turn can be used to predict various thermodynamic properties, such as excess enthalpy, Gibbs free energy, and phase equilibria.

Table 1 UNIFAC parameters for selected species

Functional group	**Volume parameter, r_i**	**Surface area, q_i**
CH	0.4469	0.228
CH_2	0.6744	0.54
CH_3	0.9011	0.848
OH	1.0	1.2
H_2O	0.92	1.4

UNIFAC model is based on a number of specific parameters for the groups that constitute a compound or a mixture. Among those parameters are functional group's volume, r_i, and surface area, q_i. Besides r_i and q_i the within the UNIFAC framework the interaction energies between different functional groups are defined. The values for interaction energies between groups and surface area and volume for each functional group could be found in the literature (Jain et al., 2017; Kang et al., 2011; Singh and Pathanjali, 1987). The values for selected species are given in Table 1, for volume and surface area parameter of each group, and Table 2 for interaction energies between groups. and surface area parameter of each group, and Table 2 for interaction energies between groups. A compound or a mixture in turn is represented by a combination of groups as well as the number of occurrences of the functional group on each compound or mixture v_g, Table 3.

Table 2 Interactions energies between species in UNIFAC model

$u_{ij},\ j \rightarrow$ $i \downarrow$	CH	CH_2	CH_3	OH	H_2O
CH	0	3.446	-11.12	161.7	90.49
CH_2	38.81	0	-35.36	240.9	61.11
CH_3	61.13	86.02	0	391.5	206.6
OH	-44.85	1.163	-30.48	0	-41.11
H_2O	-223.9	-25.38	-83.98	38.89	0

The interaction energy between species i and j, denoted as ΔU_{ij}, is fundamental to the UNIFAC model and is defined as:

$$\Delta U_{ij} = U_{ij} - U_{jj} \qquad 1$$

where U_{ij} is the interaction energy between species i and j, and U_{jj} is the self-interaction energy of species j. This asymmetry arises because the molecular interactions between different species are not necessarily reciprocal. For example, the interaction between a polar and a nonpolar molecule could differ from the reverse interaction.

In a mixture of different chemical species, the differences in interaction energies lead to a "tendency" of some species, j, to be surrounded by other species, i. In this work we define the tendency B_{ij}, which reflects the propensity of a species j to be surrounded by species i in the liquid phase. Mathematically, B_{ij} is expressed as:

$$B_{ij} = \frac{q_i}{q_j} \exp\left(-\frac{\Delta U_{ij}}{RT}\right) \qquad 2$$

where q_i and q_j are the surface area parameters of species i and j, respectively, and RT is the product of the gas constant and temperature. The exponential term, $\exp\left(-\frac{\Delta U_{ij}}{RT}\right)$, captures the influence of the interaction energy on the local structure of the mixture.

The structure of the liquid phase can thus be reconstructed by calculating these tendencies, which, in turn, allow for the determination of surface area fractions for $i-i$ and $i-j$ systems:

$$q_{ii} = \frac{1}{1+\sum_{i \neq j} B_{ij}} \qquad 3$$

$$q_{ij} = q_{ii} B_{ij} \qquad 4$$

An example of such a structure calculation for a mixture of water (W) with glycerol (G) is presented in Figure 3, where surface area fractions, qij, for pairs of OH-H_2O, H_2O -H_2O and OH-OH depending on the fraction of water in the mixture are presented. These formulas imply that if all interaction energies are zero ($B_{ii} = 1$ because $\Delta U_{ii} = 0$), the surface area would be equally split among different species, reflecting a uniform distribution and, fundamentally, describing regular solutions. However, when interaction energies between different species are non-zero the surface area fractions are affected by the energy differences, leading to a structured arrangement that mirrors the interaction tendencies.

This concept of tendency is pivotal in this work for understanding the structural organization of species within a mixture. The "local area fractions" describe how different functional groups are distributed on the molecular surface. When the interaction energy between species i and j is favourable (i.e., ΔU_{ij} is

negative), species j has a higher tendency to be surrounded by species i. Conversely, if the interaction is unfavourable (ΔU_{ij} is positive), the presence of species i around j is less likely.

This provides a complete set of surface area fractions which can be used to define the property of interest. The basic form, suggested in this work, to define a property of interest, p, is expressed in the following form:

$$p = \sum_i x_i p_i + \sum_i \sum_j q_{ji} \cdot p_{ji} \qquad 5$$

In the equation 5 the x_i is the mole fraction of a group in the chemical system. The first sum in the eq. 5 corresponds to an ideal contribution and the second sum represents non-ideal, excess contribution to the property of interest. It can be seen from the eq. 5 that the ideal part is basically molar fraction weighted sum of groups' contribution to the property, p_i. The excess non-ideal contribution is represented by p_{ij} and is weighted by the surface area fractions for $i - j$ pairs.

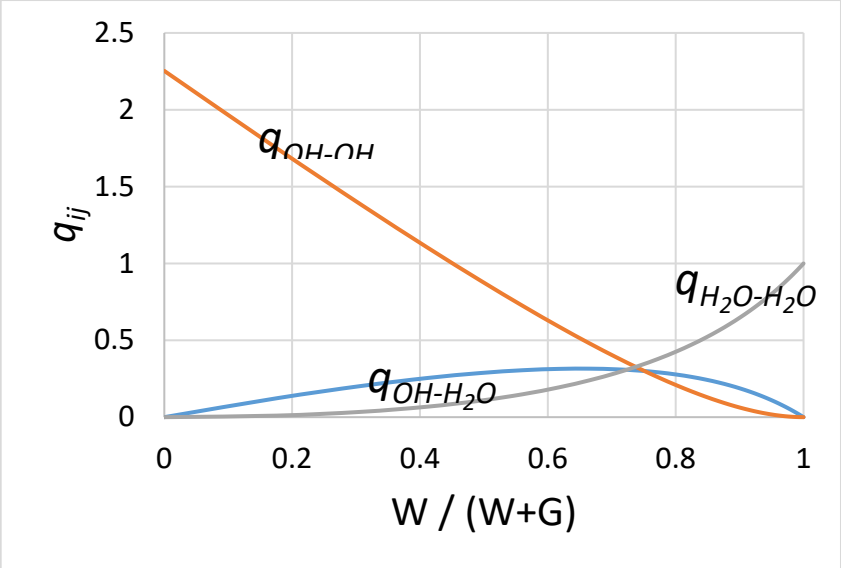

Figure 3: Surface area fractions, *q_{ij}, for the water (W) / glycerol (G) system*

Besides the fact that this algorithm allows for prediction of physical properties of mixed systems it also efficiently reconstructs the structure of the liquid phase in terms of local area fractions and provides insights into the structure of a liquid phase of interest.

2.1.1 Results

In this work the developed approach has been used to calculate the refractive index and molar volume. Such a set of properties is dictated by the research needs in the field of experimental thermo-hydraulics where optical methods are used extensively to study buoyant flows for liquids with different densities and viscosities and where optical methods, like particle image velocimetry (PIV), are being extensive used (Clément et al., 2018; Krohn et al., 2018; Valori et al., 2024; Zhang et al., 2017).

Considering this, we set a goal of attempting to predict refractive indexes of mixed systems using with significant accuracy to be able to speed up the search of possible candidates for the research fluid and medium for such kinds of experiments.

Using the calculated surface area fractions from Eqs. 3 and 4, we can estimate refractive index of the mixture by modifying Eq. 5 to calculate the refractive index as:

$$n = \sum_i x_i n_i + \sum_i \sum_j q_{ji} \cdot n_{ji} \qquad 6$$

where x_i is the mole fraction of group i, n_i reflects ideal contribution to the refractive index of the mixture from the functional groups that compose the mixture, and n_{ji} is the «excess» refractive index contributions that arise from the $i - j$ interaction. Table 3 Functional groups of compounds

	CH	CH_2	CH_3	OH	H_2O
Water	0	0	0	0	1
Isopropanol	1	0	2	1	0
Glycerol	1	2	0	3	0
Ethanol	0	1	1	1	0
Propanol	0	2	1	1	0
Methanol	0	0	1	1	0

Table 4 and

Table 5 provide information on ideal and excess contributions to the refractive index using equation 5. It should be noted that the ideal contribution to the refractive index contains also the temperature correction, and the ideal contribution can be then calculated as follows:

$$n_i = n_i^o + n_i^T \cdot T \qquad 7$$

Table 3 Functional groups of compounds

	CH	CH_2	CH_3	OH	H_2O
Water	0	0	0	0	1
Isopropanol	1	0	2	1	0
Glycerol	1	2	0	3	0
Ethanol	0	1	1	1	0
Propanol	0	2	1	1	0
Methanol	0	0	1	1	0

Table 4 Ideal contributions to the refractive index

FG	n_i^o	n_i^T
CH	-0.036855	3.9746 e-3,
CH_2	-1.55246	1.10085 e-4
CH_3	-0.55569	1.17372 e-3
OH	-0.75553	-1.8993 e-3
H_2O	5.50603	-1.651 e-4

Table 5 Excess contributions to the refractive index

n_{ij} $j \rightarrow$ $i \downarrow$	CH	CH_2	CH_3	OH	H_2O
CH	0.773428	-3.35332	2.416407	-3.60084	-1.97339
CH_2	-3.35332	1.514359	-2.3244	4.543135	0.045617
CH_3	2.416407	-2.3244	-2.9775	3.836992	-0.90921
OH	-3.60084	4.543135	3.836992	0.603036	-0.81355
H_2O	-1.97339	0.045617	-0.90921	-0.81355	-4.12371

Since the information on the interaction energy between species i and j, ΔU_{ij} is known from the literature (Jain et al., 2017; Kang et al., 2011; Singh and Pathanjali, 1987), the task was to optimize the n_i^o, n_i^T and n_{ji} and parameters to available experimental data for a set of groups of interest and then test the optimized parameters to predict refractive index of systems for which no optimization has been performed.

In this work it has been decided to optimize the n_i^o, n_i^T and n_{ji} parameters to a set of binary systems and then test these parameters on ternary systems to see how well the developed approach can predict properties of multicomponent systems and whether it would be able to predict properly refractive index of multicomponent mixtures.

Refractive index of multicomponent systems

The water-isopropanol-glycerol systems has been selected as a first test system for our research due to the fact that accurate data for the refractive index of involved binary sub-systems (water-isopropanol, water-glycerol and isopropanol-glycerol) are available in the literature. The calculated ternary diagram for water-isopropanol-glycerol system is given in the Figure 4.

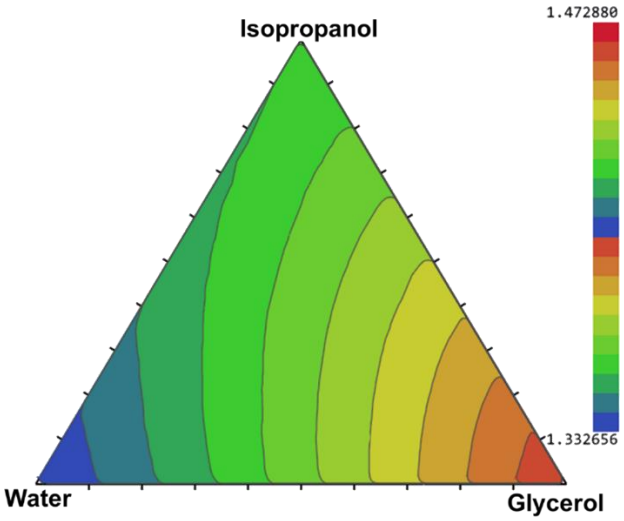

Figure 4: Calculated ternary diagram of refractive index for the water-isopropanol-glycerol system

To better demonstrate accuracy of the developed approach in predicting properties of multicomponent systems we have also performed calculations of the refractive index for the water-isopropanol-glycerol system using simple mass fraction weighted value, Equation 8, for the refractive index and calculated deviations from between the calculated values and experimental values provided in the literature (Krohn et al., 2018).

$$n_w = \sum_i w_i n_i^w \qquad 8$$

w_i is the weight fraction of the compound in the ternary mixture, n_i^w is a refractive index of pure compound *i*.

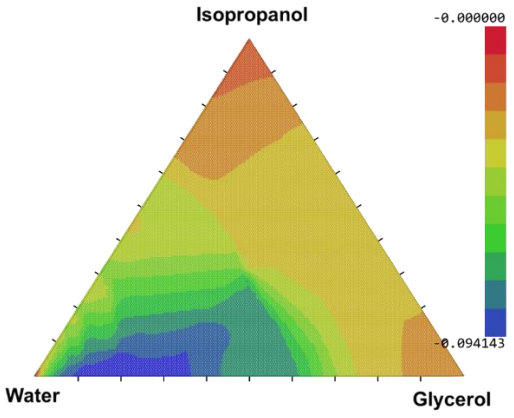

Figure 5: Difference between calculated and experimental values of refractive index using simple weight fraction weighted values

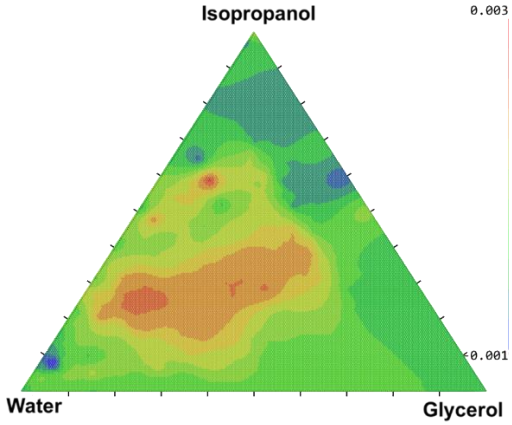

Figure 6: Difference between calculated and experimental values of refractive index using developed model

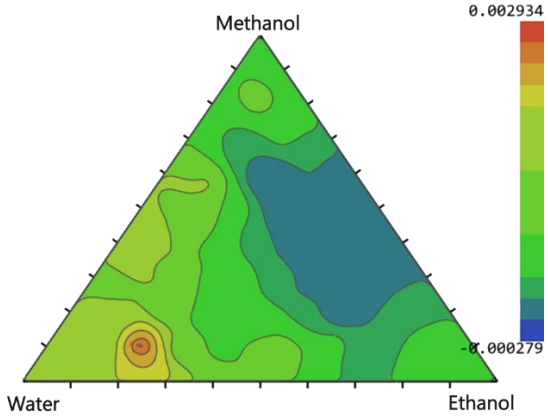

a) water-methanol-ethanol system

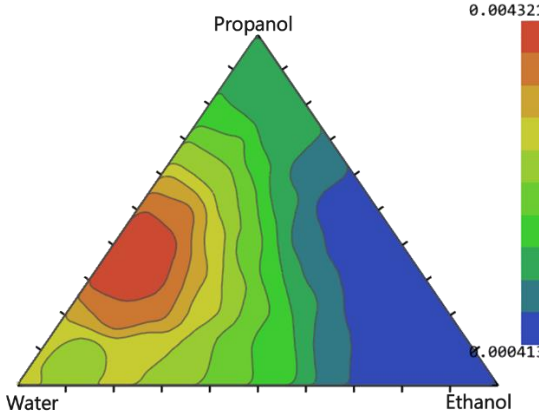

b) water-propanol-ethanol system

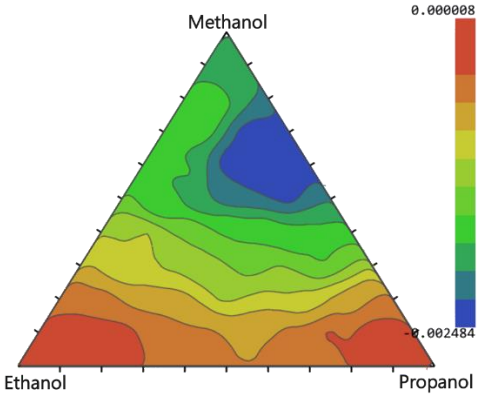

c) ethanol-methanol-propanol system

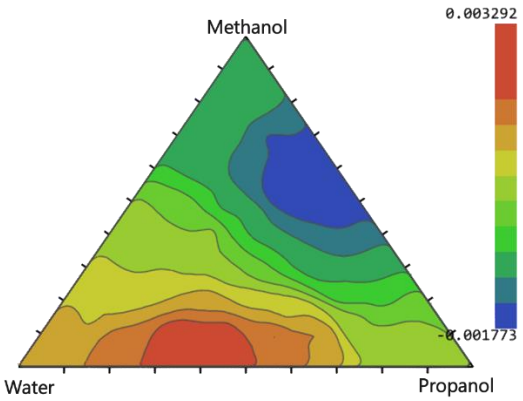

d) water-propanol-methanol system

Figure 7: Difference between calculated and experimental values of refractive index using developed model for different ternary systems

It is clearly seen from the Figure 5 and Figure 6 that application of the developed model to calculate refractive index of a complex ternary system reduces the total deviation between calculated and experimental values from 0.09 to about 0.003, which is a significant improvement in accuracy.

The following set of Figure 7a-d, also demonstrates the deviations between experimental results and calculated values of the refractive index for a set of ternary systems. As it can be seen from these figures that the developed model for calculating refractive index allows for predicting refractive index of complex multicomponent systems with high degree of accuracy.

Molar volume of multicomponent systems

Besides refractive index of multicomponent systems it is of great interest to be able to calculate densities of multicomponent systems as well. This, is it has been mentioned above, would serve as a source of information for researchers that are interested in such experimental methods as Particle Image Velocimetry when applied to buoyant flows and jets.
In this work the developed approach to calculating molar volumes has been used in the following form:

$$v = \sum_i x_i v_i + \sum_i \sum_j q_{ji} \cdot v_{ji} \qquad 9$$

where x_i is the mole fraction of group i, v_i reflects ideal contribution to the molar volume of the multicomponent system from the functional groups, and v_{ji} is the «excess» molar volume contributions that are caused by the $i-j$ interaction. The ideal contribution, like in the case with refractive index, is temperature dependent and has the following form:

$$v_i = v_i^o + v_i^T \cdot T \qquad 10$$

Table 6 and Table 7 provide parameters for the molar volume model.

Table 6 Ideal contributions to the molar volume

FG	v_i	v_i^T
CH	-159.793	0.395681
CH_2	304.1282	-0.76831
CH_3	68.66302	-0.35644

OH	-157.452	0.393469
H_2O	-58.5977	0.007095

Table 7 Excess contributions to the molar volume

v_{ij} $j \rightarrow$ $i \downarrow$	CH	CH_2	CH_3	OH	H_2O
CH	4.89759	5.697112	36.41886	13.19421	52.20851
CH_2	5.697112	-44.5798	-78.6198	22.39728	-21.4957
CH_3	36.41886	-78.6198	100.2774	67.35523	68.00965
OH	13.19421	22.39728	67.35523	19.90187	60.80729
H_2O	52.20851	-21.4957	68.00965	60.80729	74.58728

Together with the refractive index, information on density, that easily derived from molar volume, ca be used to look for potential candidates for experimental investigations where systems with the same, or very close, refractive index but as high as possible difference in densities are required. In this work we performed such a search for potential candidates on a ternary water-glycerol-isopropanol diagram. The idea is to find two concentrations that would have very close refractive index and pronounced densities and at the same time would, when mixed, preserve refractive index. In this way when the experiments will be performed the mixing such liquids will cause insignificant variations in refractive index and therefore will permit applications of such optical methods as PIV.

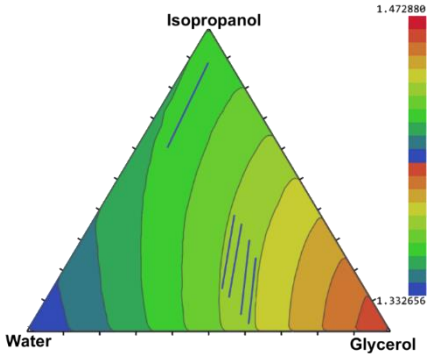

Figure 8: Potential candidates for PIV measurements

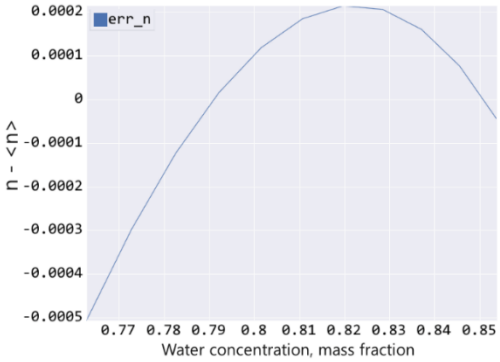

Figure 9: Potential candidates for PIV measurements

Figure 8 demonstrates a number of found potential candidates, depicted with blue lines, that have a predicted density difference of at least 8% along the line. In the Figure 9 the variation in deviation of refractive index from its average values along one of the found potential lines is given. It can be seen that the maximum deviation of the refractive index from the average value is about 0.0005, and can be reduces if the concentration range is slightly reduced.

In conclusion, preliminary calculations using this algorithm have shown that the predicted refractive indices closely match experimental values, demonstrating the accuracy of the method. Additionally, the algorithm has been applied to other properties, such as molar volume, with similarly promising results. These findings suggest that the proposed method can be a valuable tool for predicting the properties of complex liquid mixtures, particularly in cases where experimental data is limited or unavailable.

The proposed algorithm efficiently reconstructs the structure of the liquid phase in terms of local area fractions and provides accurate predictions of mixture properties. The initial results are promising, indicating the potential for broader applications of the UNIFAC model in predicting the properties of complex liquid mixtures. Future work will focus on further validating the algorithm with a wider range of systems and exploring potential modifications to enhance its accuracy.

2.2 Experimental Facility: MiniDestrojer

The MiniDestrojer (DEnsity Stratified Turbulent ROund free Jet ExpeRiment) facility has been designed and built to investigate the mixing of buoyant jets in uniform and stratified environments. The facility is shown in Figure 10. The test section of the MiniDestojer setup consists of a tank of dimensions of 300 x 300 x 300 mm. Inside the tank, a nozzle is located to guide the injection capillary. Tests are possible with a 2mm and a 3mm inner-diameter injections respectively. A high-speed Particle Image Velocimetry (PIV) system has been acquired to capture the turbulent jet flow injected from the capillariy at the bottom of the tank. To accurately adjust the positioning of the PIV light sheet in the center of the capillary, a custom-made PIV calibration target has been developed. The target can be rotated continuously around the Z-Axis and can be tilted with adjustment screws around the two other axis by 2.5°, and it has been designed to perfectly align with the center of the capillary injection.

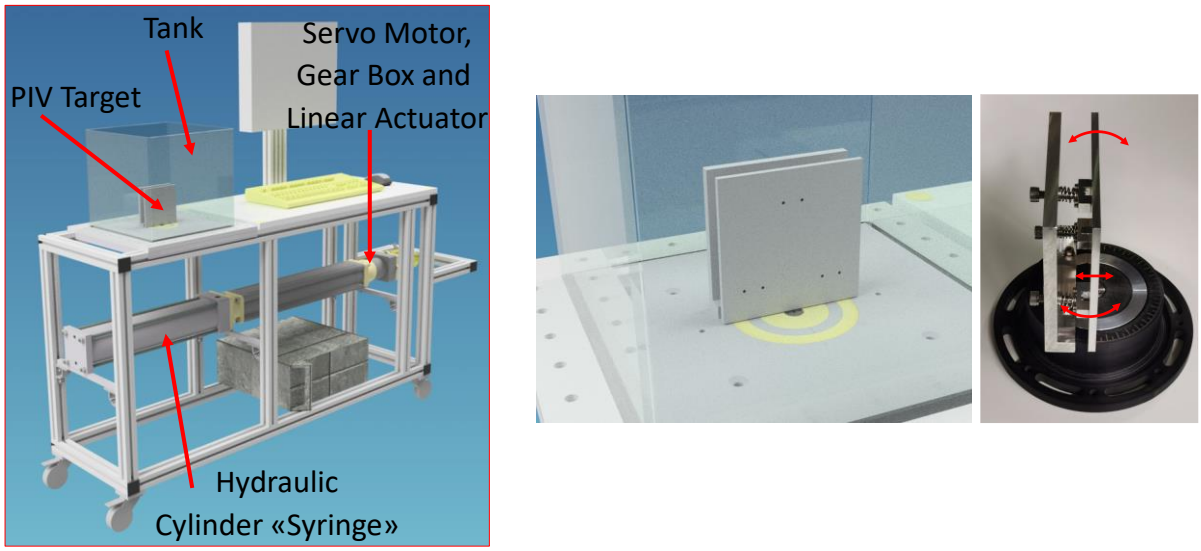

Figure 10: MiniDistrojer experimental setup (left), zoom of test section with calibration target (center) and detail of PIV calibration target (right).

The test section is located on a cart constructed with aluminium profiles. In the lower part of the cart the injection system is located comprising of a servo motor, which drives over a planetary gear box a linear electro cylinder, which actuates a hydraulic cylinder, acting as a “syringe” do dispense the desired amount of liquid to be injected via the capillary into the tank. The hydraulic cylinder is designed to reach injection velocities of up to 17 m/s, and corresponding Reynolds numbers up to 56’000.

Figure 11: MiniDESTROJER Facility with instrumentation for 3D-PIV and LIF measurements.

The fully commissioned experimental facility is shown in Figure 11. The instrumentation includes four high-speed CMOS cameras and two light sources: a high-speed Nd laser and a blue LED. This setup supports Particle Image Velocimetry (PIV), Particle Tracking Velocimetry (PTV), Laser-Induced Fluorescence (LIF) measurements, and simultaneous PIV or PTV with LIF. The tested combinations of experimental techniques are summarized in Table 8. Selected results from the facility commissioning runs are presented in Figure 12.

Table 8: Summary of the tested experimental techniques

Techniques	Cameras used	Illumination source
Planar PIV + LIF	Two, one for PIV, one for LIF	Laser (sheet)
Stereo PIV + LIF	Three, two for stereo PIV, one for LIF	Laser (sheet)
Tomo PIV + LIF	Four, three for tomo PIV, one for LIF.	LED (volume) for tomo PIV and laser (sheet) for LIF
4D PTV (with the Shake the Box algorithm) + LIF	Four, three for PTV, and one for LIF.	LED (volume) for 4D PTV and laser (sheet) for LIF

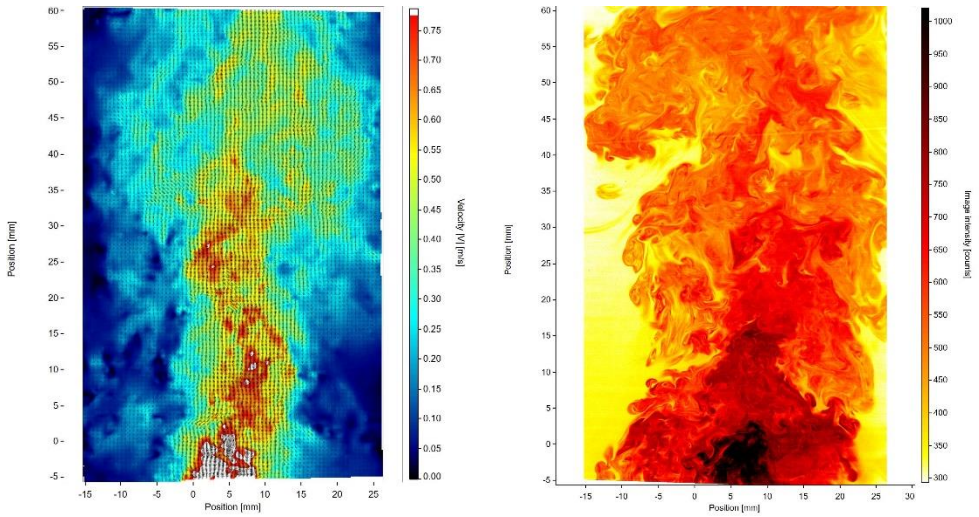

Figure 12: Instantaneous velocity field from PIV measurements (Left) and. Flow visualization from LIF measurements (Right), performed at Re = 10000.

2.3 Results

2.3.1 In-depth analysis of previously obtained experimental data.

Experiments on the mixing of buoyant jets in both uniform and stratified environments have been analyzed. The main objective is to generate data and analyses that can evaluate the predictive capabilities and limitations of current CFD models. Practical CFD models are based on the Reynolds-Averaged Navier-Stokes (RANS) approach, in which the time-dependent variables in the Navier-Stokes equations are decomposed into a time-averaged component (mean flow field) and a fluctuating component. For example, the instantaneous velocity $\boldsymbol{u}_j$ is decomposed into its mean value $\overline{u_j}$ and a fluctuation u_j' around the mean$\boldsymbol{u}_j = \overline{u_j} + u_j'$). Using Einstein notation, the governing equations describing fluid motion can be expressed as follows:

$$\frac{\partial \rho}{\partial t} + \frac{\partial (\rho \overline{u}_j)}{\partial x_j} = 0, \tag{11}$$

$$\frac{\partial (\rho \overline{u}_i)}{\partial t} + \frac{\partial}{\partial x_j}\left(\rho \overline{u_i u_j}\right) = \frac{\partial \rho}{\partial x_i} + \frac{\partial}{\partial x_j}\left[\eta\left(\frac{\partial \overline{u}_i}{\partial x_j} + \frac{\partial \overline{u}_j}{\partial x_i}\right) - \rho \overline{u_i' u_j'}\right] + g_j(\rho - \rho_0), \tag{12}$$

$$\frac{\partial (\rho \bar{c})}{\partial t} + \frac{\partial}{\partial x_j}\left(\Gamma \frac{\partial c}{\partial x_j}\right) - \frac{\partial}{\partial x_j}\left(\rho \overline{u_j' c'}\right), \tag{13}$$

where, ρ represents the density field, **c** the concentration scalar field, η the dynamic viscosity, and Γ the diffusivity. Due to the Reynolds decomposition, two additional terms appear in the Reynolds-averaged Navier-Stokes (NS) equations, which are absent in the original instantaneous NS equations: the cross-correlation of velocity component fluctuations $\overline{u_i' u_j'}$, also known as Reynolds stresses, and the turbulent fluxes $\overline{u_j' c'}$, which represent the correlation between the fluctuations of velocity components and the concentration scalar. Measuring these terms is essential for assessing the performance of CFD models. PIV and PLIF are typically used to measure velocity and concentration fields with high spatial and temporal resolution. However, in cases involving density differences, such as buoyant jets, a non-uniform refractive index arises in the flow field. This leads to a phenomenon called Schlieren, caused by optical inhomogeneities (varying refractive indices) in transparent materials, which results in blurred images and biased or erroneous measurements of velocity and concentration fields when using optical techniques like PIV and PLIF. To prevent distortion of the laser sheet used to illuminate the flow and the

light scattered by the tracing particles due to density changes which also cause change in index of refraction, it is crucial to match the refractive indices of the solutions used in experiments. To address this, a novel Refractive Index Matching (RIM) technique was developed and demonstrated by the project PIs (see Krohn et al., 2018; Qin et al., 2018). This technique significantly extends the applicability of PIV/PLIF beyond the previously recorded 3% range of density difference in the literature. Two sets of experiments have been analyzed with respect to the Reynolds (Re) and Richardson (Ri) numbers. These two dimensionless numbers are defined as follows:

$$\mathrm{Re}(x_0, y) = \frac{DV(x_0,y)}{\nu(x_0,y)}, \mathrm{Ri} = gD\frac{\rho_{env.}-\rho_{jet}}{\rho_{jet}V_0^2}, \qquad 14$$

This analysis allows for the characterization of the relative importance of buoyancy forces versus momentum forces. In this context, D is the diameter of the jet's orifice, $V(x_0, y)$ is the time-averaged vertical velocity, υ is the kinematic viscosity of the fluid along the jet axis $(x = x_0, y)$, g is the magnitude of the gravitational acceleration, $\rho_{env.}$ is the mass density of the surrounding environment, ρ_{jet} is the mass density of the jet at the orifice, and V_0 is the jet's velocity at the orifice. The operational conditions for the experiments analyzed are listed in Table **9**, and the configurations are illustrated in Figure 13. A detailed discussion of the results is provided by Valori et al. (2023); here, only a brief summary is included. As shown in Table 9, experiments were conducted for turbulent flows (Re = 10,000), laminar flows (Re = 2000), and transitional flows in between (Re = 4000). Experiments D029 to D050 correspond to uniform jets in a uniform environment with no density difference and serve as a reference for studying buoyancy effects. Experiments D033 to D036 and D047 to D052 involve buoyant jets in uniform environments with 3.16% and 8.6% density differences, respectively. Experiments D042 and D043 examine buoyant jets in stratified environments. Notably, measurements with an 8.6% density difference were made possible only through the novel RIM technique developed by the PIs, as described in Krohn et al. (2018).

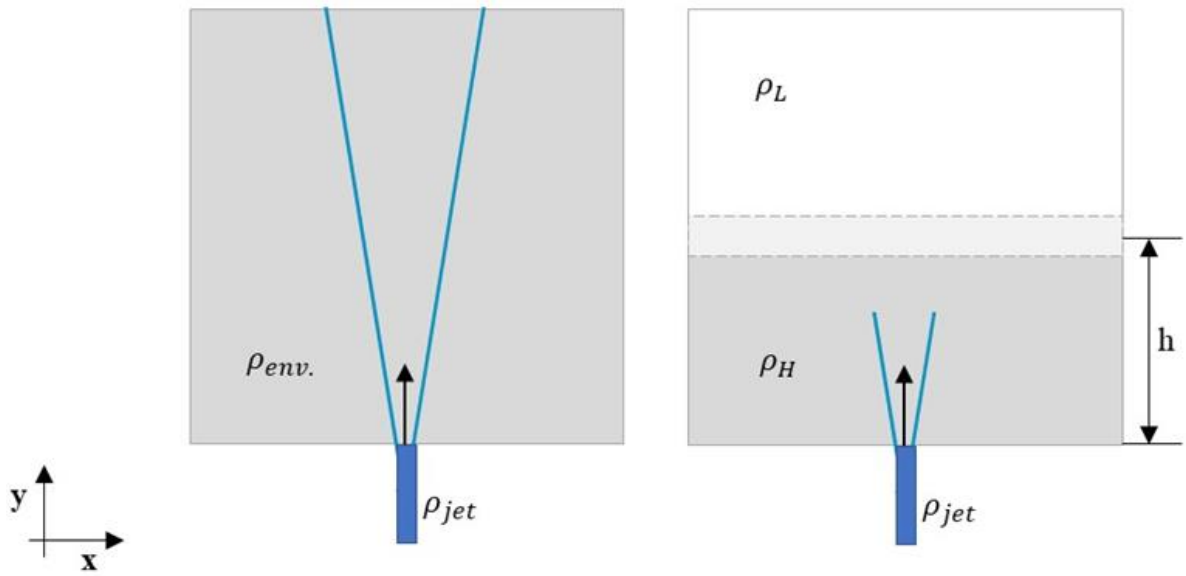

Figure 13: Buoyant jet configuration. Uniform environment (left) and stratified environment (right).

Table 9: Summary of experimental conditions analyzed.

Case	[m/s]	ρ_{jet} [kg/m^3]	ρ_{env} [kg/m^3]	$\Delta\rho$ [%]	T [°C]	Re	Ri [×10^{-5}]
D029	5.990 ± 0.004	1012.0 ± 10.1		0	20.4 ± 0.1	10000	
D030	2.460 ± 0.002	1012.0 ± 10.1		0	20.4 ± 0.1	4000	
D031	5.530 ± 0.004	1044.0 ± 10.4		0	20.0 ± 0.1	10000	
D032	2.300 ± 0.002	1044.0 ± 10.4		0	20.0 ± 0.1	4000	
D045	9.060 ± 0.006	1011.0 ± 10.1		0	19.2 ± 0.1	4000	
D046	4.220 ± 0.003	1011.0 ± 10.1		0	19.3 ± 0.1	2000	
D049	9.060 ± 0.006	924.3 ± 9.2		0	18.4 ± 0.1	4000	
D050	4.220 ± 0.003	924.3 ± 9.2		0	18.6 ± 0.1	2000	
D033	5.990 ± 0.004	1012.0 ± 10.1	1044.0 ± 10.4	3.16	20.4 ± 0.1	10000	1.73
D034	2.460 ± 0.002	1012.0 ± 10.1	1044.0 ± 10.4	3.16	20.4 ± 0.1	4000	10.3
D035	5.530 ± 0.004	1044.0 ± 10.4	1012.0 ± 10.1	3.16	20.0 ± 0.1	10000	-1.97
D036	2.300 ± 0.002	1044.0 ± 10.4	1012.0 ± 10.1	3.16	20.5 ± 0.1	4000	-11.4
D042	5.990 ± 0.004	1012.0 ± 10.1	Stratification		18.1 ± 0.1	10000	
D043	2.460 ± 0.002	1012.0 ± 10.1	Stratification		19.0 ± 0.1	4000	
D047	9.060 ± 0.006	1011.0 ± 10.1	924.3 ± 9.2	8.60	19.3 ± 0.1	4000	-2.05
D048	4.220 ± 0.003	1011.0 ± 10.1	924.3 ± 9.2	8.60	19.7 ± 0.1	2000	-9.45
D051	9.060 ± 0.006	924.3 ± 9.2	1011.0 ± 10.1	8.60	18.5 ± 0.1	4000	+2.00
D052	4.220 ± 0.003	924.3 ± 9.2	1011.0 ± 10.1	8.60	18.8 ± 0.1	2000	+10.3

Figure 14 presents the vertical mean velocity profiles at the jet axis location $y/D = 40$, normalized by the initial velocity (V_0) for all experiments listed in Table 9. Error bars are shown based on the uncertainty estimates of Qin et al., 2018 . The radial velocity profiles collapse across all experiments, indicating no significant influence from the Reynolds and Richardson numbers. This observation aligns with the findings of Hrycak et al.1974, who reported that for an axisymmetric jet, the radial velocity profile—when normalized by the centerline velocity—is largely independent of the Reynolds number within the turbulent flow region. The Full Width at Half Height (FWHH) of the vertical velocity profile exhibits a consistent slope across all experiments, with the exception of case D043 (Figure 15). This case, alongside D042, involves a two-layer stratified environment with a distinct interface (see Table **9**).

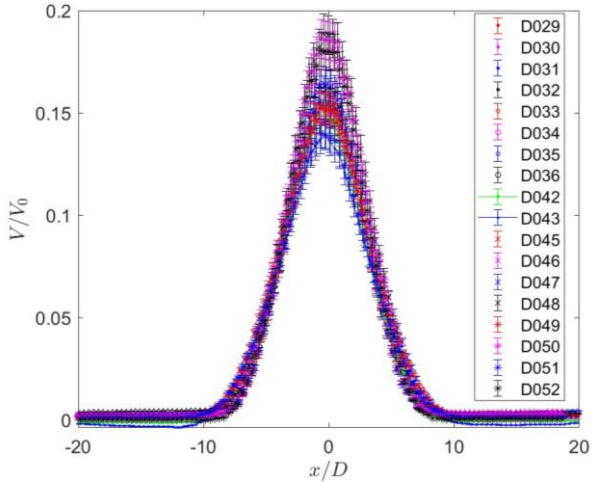

Figure 14: Spanwise velocity at $\frac{y}{D} = 40$, with error bars.

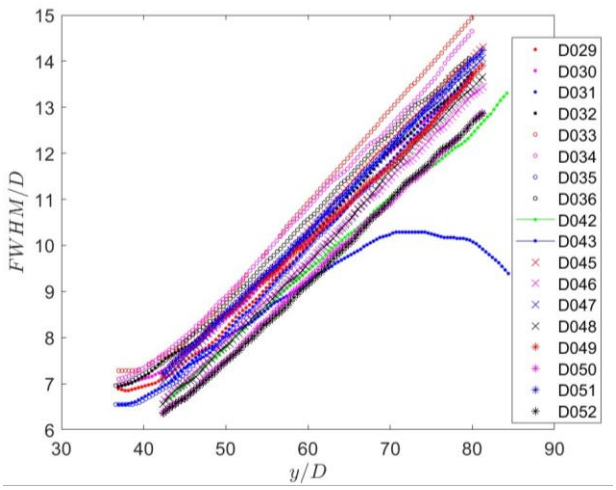

Figure 15: Full Width at Half Maximum (FWHM) of the mean velocity profile.

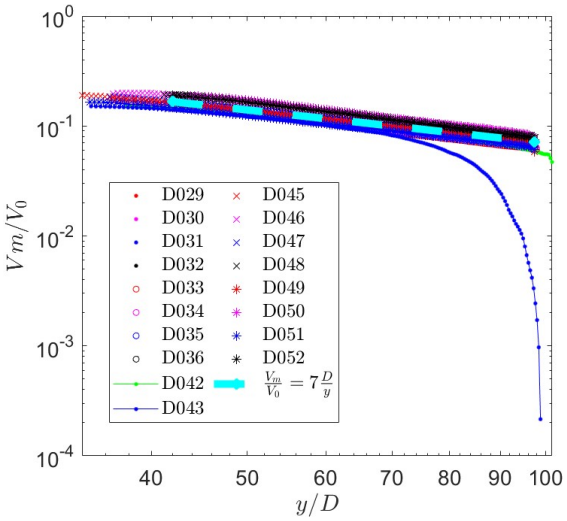

Figure 16: Mean velocity on the axis of a turbulent jet as a function of distance from the jet orifice.

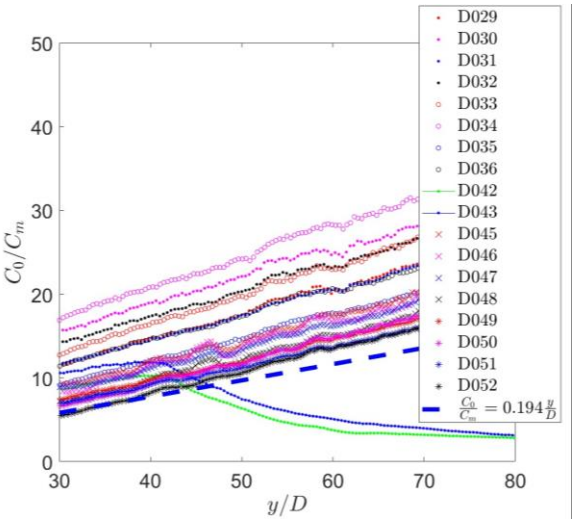

Figure 17: Mean concentration on the axis of a turbulent jet as a function of distance from the orifice.

Notably, D043 has a lower Reynolds number (Re = 4000) compared to D042 (Re = 10000), resulting in reduced momentum. Consequently, the jet width in D043 diverges from that of other experiments beyond the interface at approximately $\frac{y}{D} = 60$. The mean velocity along the jet axis, normalized by the orifice velocity (V_m/V_0), shows a consistent slope for all cases, except for D043 (Figure 16), where the jet velocity decreases sharply at approximately $\frac{y}{D} = 70$. For cases without stratification, as well as the stratified case with a high Reynolds number, the slope of V_m/V_0 as a function of distance from the orifice agrees well with reference values from previous turbulent jet experiments (List et al.1982). Figure 15 and Figure 16 indicate that in stratified environments, a jet with a high Reynolds number, such as D042 (Re=10000), has sufficient momentum to penetrate the upper fluid layer. In contrast, when the Reynolds number is lower, as in D043, the jet behaves similarly to a fountain, reaching a maximum height before descending back to the density interface, interacting with both the layer and the upward flow. Additionally, the inverse of the mean tracer concentration along the jet axis, multiplied by the orifice concentration (C_0/C_m), displays a consistent slope across jets with and without buoyancy, except in the two stratified cases (Figure 17). In these stratified cases, tracer concentration increases below the interface location. For cases in a uniform environment, the experimental slopes align well with those from previous studies in the literature (List et al.,1982).

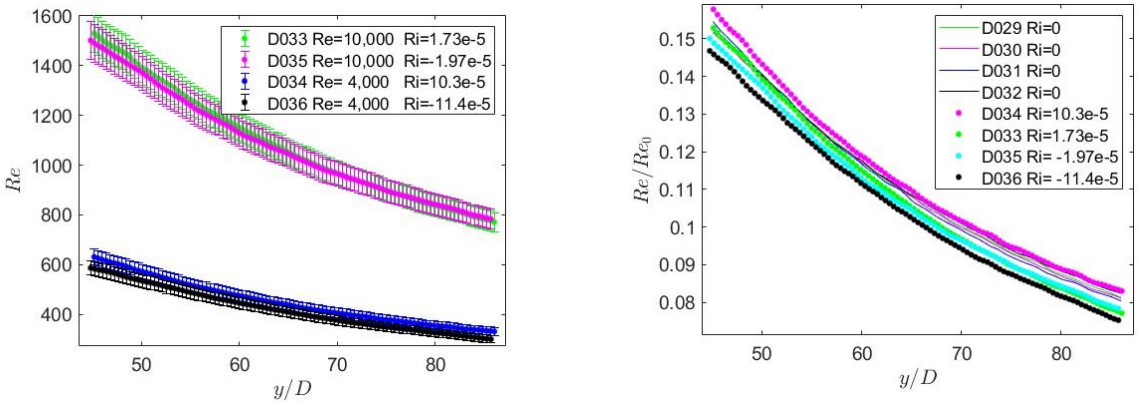

Figure 18: Re number at the jet's centerline for experiments D033 to D036 (left) and normalized Re at the jet centerline (right).

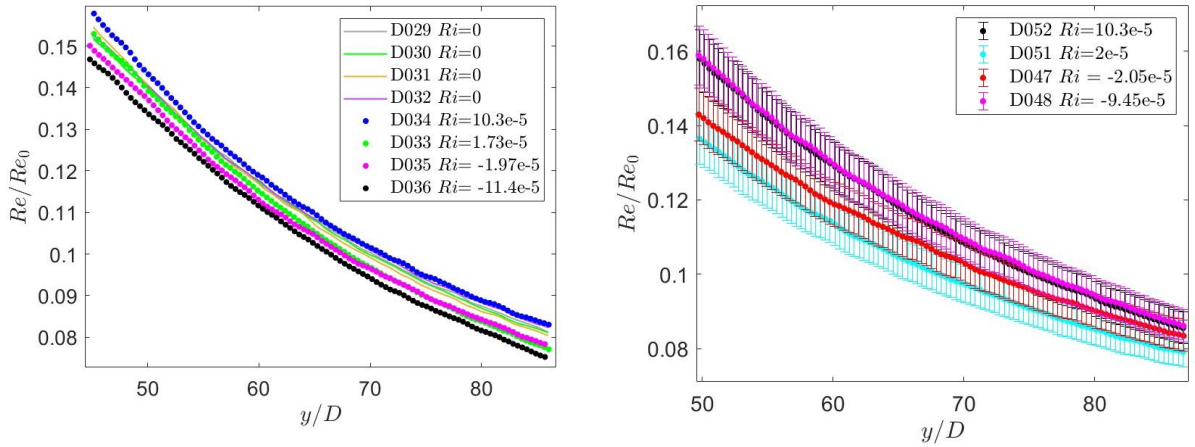

Figure 19: Reynolds number at the jet's centerline normalized by the Reynolds number at the orifice, for experiments D029, to D036 (left) and for experiments D047 toD052 (right).

Figure 18 (left)illustrates the evolution of the Reynolds number along the jet axis for both positively and negatively buoyant jets with varying orifice velocities. The local Reynolds and Richardson numbers are computed using equations (4) The kinematic viscosity used to determine the local Reynolds number is based on tracer concentration measurements from LIF experiments (Qin et al.2019). From Figure 18 (left), it is evident that the Reynolds number along the jet axis depends on the Reynolds and Richardson numbers at the orifice. Specifically, cases D033 and D035, which have a higher initial Reynolds number (Re = 10000), exhibit greater Reynolds numbers along the axis compared to cases D034 and D036 (Re = 4000). Furthermore, cases D033 and D034, characterized by a positive initial Richardson number (Ri_0), show higher Reynolds values along the axis than cases D035 and D036, respectively, for the same initial Reynolds number. These findings align with the observations of Nathan et al.2006, who reported that jet inlet conditions significantly influence both the near-field and downstream flows by shaping the turbulent structures that propagate from the jet nozzle throughout the flow. Figure 18 (right) presents the data from Figure 18 (left), normalized by the orifice Reynolds number (Re_0). After normalization, the Reynolds values along the axis are arranged according to the Richardson number, indicating that buoyancy positively affects jet speed. Figure 19 (left) includes four additional experiments of pure jets in a uniform environment without buoyancy (cases D029, D030, D031, and D032; see Table 9 for details). These experiments are positioned approximately between the cases with positive and negative Richardson numbers. In experiments with an 8.6% density difference (see Figure 19 (right)), no clear ordering of the Reynolds number values along the axis according to Richardson number is observed. This may be attributed to uncertainties in kinematic viscosity measurements of the two solutions used, due to the high volatility of isopropanol.

Figure 20 and Figure 21 show the Probability Density Function (PDF) of mass density for cases D033, D034, D035, and D036 at two locations along the jet axis. At each fixed y/D, the density distribution exhibits a peak and a plateau towards lower values. The peak corresponds to the density of the injected fluid, while the plateau represents the mixing region with the surrounding environment. For all cases, the PDF width at $\frac{y}{D} = 80$ is narrower than at $\frac{y}{D} = 40$, indicating improved mixing further from the jet orifice. Additionally, the maximum peak at $\frac{y}{D} = 80$ is slightly reduced, further suggesting enhanced mixing with the environment. Cases D033 and D034 (Figure 20) are characterized by a positive density difference between the jet and the environment (positively buoyant jets), while cases D035 and D036 (Figure 21) have a negative density difference. Comparing Figure 20 and Figure 21, it is evident that positively buoyant jets have narrower PDFs, suggesting that buoyancy aids in mixing. Furthermore, the PDF width is greater for case D033 than for case D034 (Figure 20) and for case D035 than for D036 (Figure 21). This is expected, as cases D034 and D036 have a lower Reynolds number than cases D033 and D035 and a higher Richardson number, indicating that increased buoyancy relative to shear further promotes mixing.

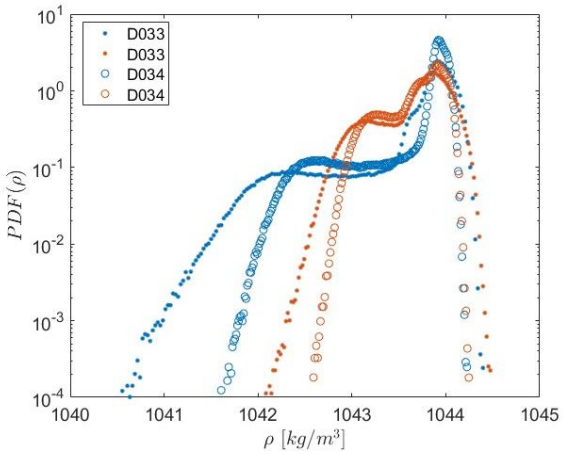

Figure 20: Probability Density Function (PDF) of the mass density of cases D033 and D034 at two locations along the jet's axis $\frac{y}{D} = 40$ (blue), and $\frac{y}{D} = 80$ (red).

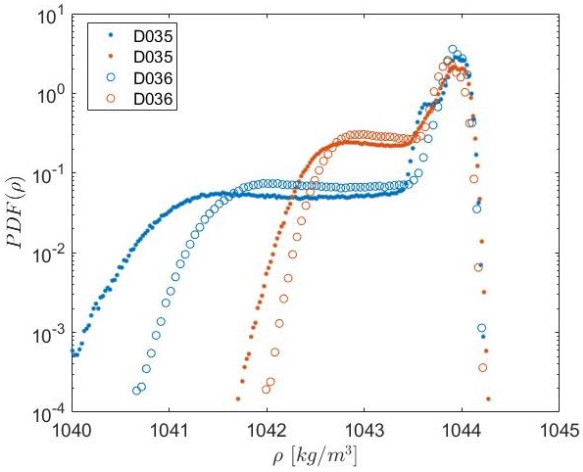

Figure 21: Probability Density Function (PDF) of the mass density of case D034 at two locations along the jet's axis $\frac{y}{D} = 40$ (blue), and $\frac{y}{D} = 80$ (red).

The turbulent shear stress is defined as $\tau(x,y) = \frac{\overline{u'(x,y,t)\cdot v'(x,y,t)}}{V^2(x_0,y)}$, where $\overline{u'(x,y,t)\cdot v'(x,y,t)}$ represents the time-averaged product of the fluctuating horizontal (u') and vertical (v') velocity components. Here, (x,y,t) denote the horizontal, vertical, and time coordinates, respectively, as shown in Figure 13, and $V(x_0,y)$ is the vertical velocity along the jet axis ($x = x_0$). Figure 22 presents the turbulent shear stress at $\frac{y}{D} = 60$ for all experiments alongside two reference studies from Wygnanski [30] and Rodi [31]. The experimental results align well with the reference data, except for case D043, which involves a stratified environment and a lower Reynolds number.

Similarly, the turbulent concentration fluxes in the vertical and horizontal directions, τ_{vc} and τ_{uc}, are defined as $\tau_{vc} = \frac{\overline{v'(x,y,t)\cdot c'(x,y,t)}}{V(x_0,y)\cdot C(x_0,y)}$ and $\tau_{uc} = \frac{\overline{u'(x,y,t)\cdot c'(x,y,t)}}{U(x_0,y)\cdot C(x_0,y)}$, where $C(x_0,y)$ is the vertical concentration and $U(x_0,y)$ is the horizontal velocity along the axis. Figure 23 and Figure 24 show the turbulent concentration fluxes τ_{vc} and τ_{uc}, respectively, at the axial position $\frac{y}{D} = 60$. Both fluxes are plotted as functions of the horizontal dimension $x/r_{1/2}$, where $r_{1/2}$ is the lateral position where the jet's vertical velocity equals half of its maximum value. In Figure 23 and Figure 24, the experimental cases show no notable differences, except for the two jets in a stratified environment (D042 and D043). For these two cases, the turbulent concentration fluxes exhibit a smaller central magnitude and a broader horizontal distribution. This suggests that the sharp stratification in the environment promotes horizontal spreading of the jet at the interface level.

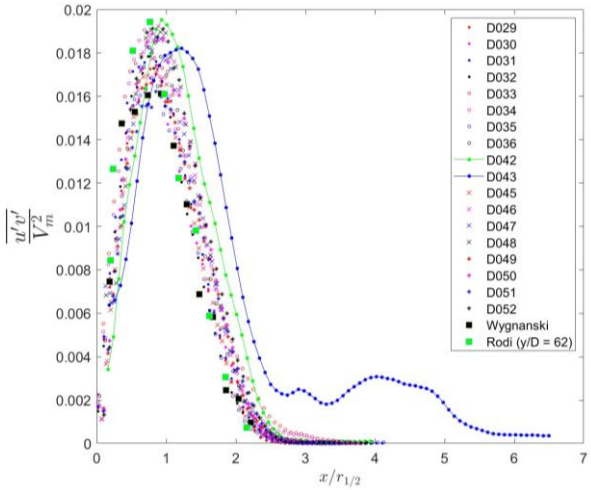

Figure 22: Turbulent shear stress at $\frac{y}{D} = 60$.

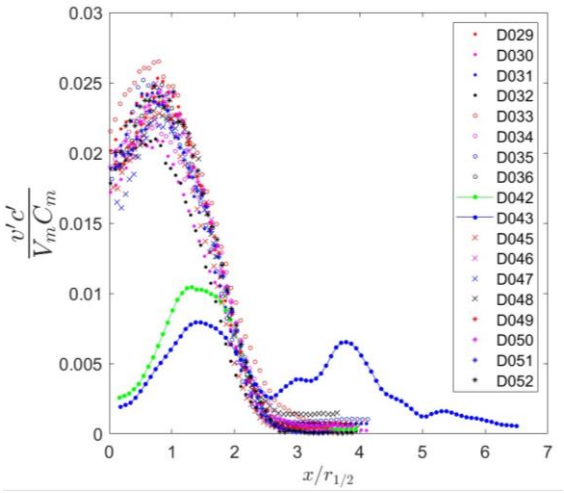

Figure 23: Turbulent concentration flux at $\frac{y}{D} = 60$.

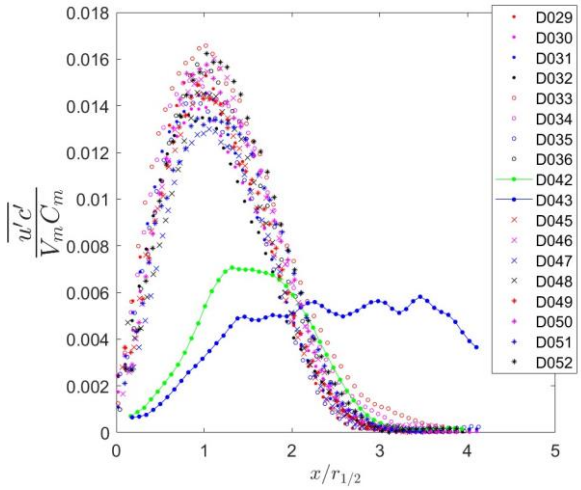

Figure 24: Horizontal turbulent concentration flux at $\frac{y}{D} = 60$.

Figure 25 presents the volume flux as a function of distance from the jet origin for all experimental cases. The volume flux is defined as the ratio between entrainment (μ) and the jet's specific mass flux at the orifice ($Q = \rho_0 V_0 A$), where ρ_0 is the mass density, V_0 is the jet velocity at the orifice, and A is the cross-sectional area. Entrainment is defined as $\mu(y) = \int_0^{L(x)} V(x,y) 2\pi x \, dx$, where V is the time-averaged vertical velocity, and L is the jet's characteristic length. In Figure 25, the volume flux is observed to be lowest for jets D042 and D043, which are injected into a stratified environment. For case D042, with a lower Reynolds number, the volume flux sharply decreases around the interface location (approximately $\frac{y}{D} \simeq 60$). Additionally, cases with the highest Richardson numbers, D034 and D052, show lower entrainment values compared to other cases in a uniform environment. Case D048, with a high negative Richardson number, has the largest volume flux. This comparison suggests that both a stratified environment and the Richardson number significantly influence the volume flux and its progression along the jet axis. Specifically, a stratified environment and a high positive Richardson number are associated with lower volume flux values. For comparison, the same plot includes a reference slope from the experimental literature review by List et al., 2082.

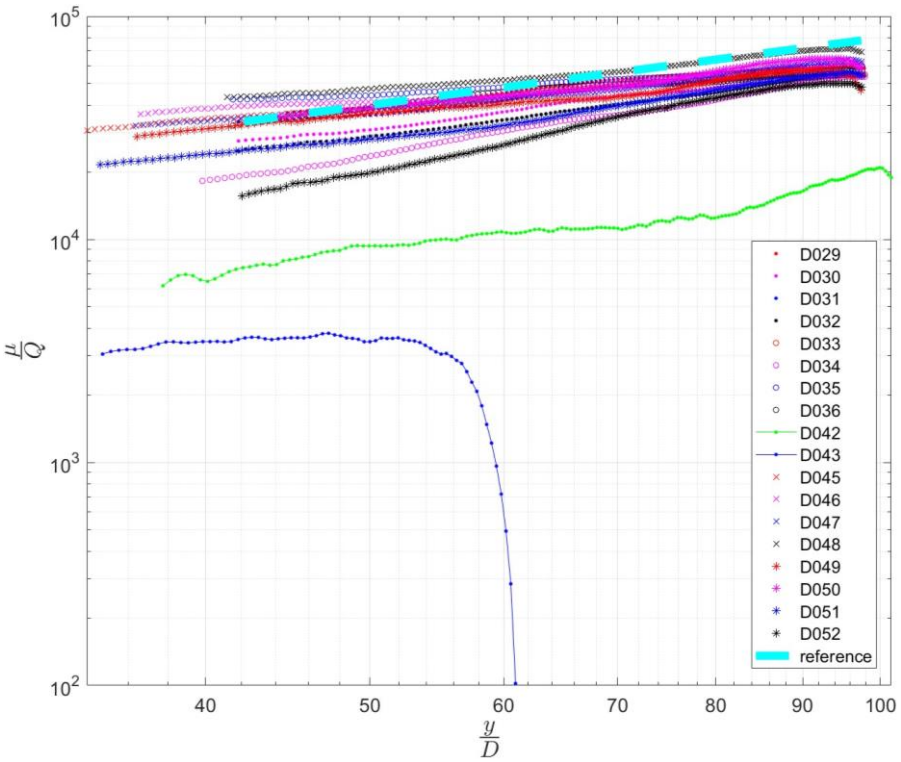

Figure 25: Volume flux as a function of distance from the jet origin for all experimental cases. (Reference line from Paladino et al., 2012).

2.3.2 In-depth analysis of newly obtained experimental data.

In previous experiments, it was observed that under certain conditions, a negatively buoyant jet can become unstable, initially collapsing before regaining structure. This behavior arises from complex interactions between buoyancy and momentum forces, particularly in stratified or density-varied environments, which affect the jet's overall stability and oscillatory motion. Such instabilities are typically investigated using 3D flow visualizations to qualitatively assess the spatial structure of the jet and measure its penetration height over time. However, refractive index inhomogeneities caused by density gradients between the jet and the surrounding environment complicate the study of liquid buoyant jets and limit the use of optical techniques for quantitative measurements. To address this, we apply a refractive index matching method, allowing high-resolution optical measurements of both velocity and concentration fields. Experiments were conducted at Froude numbers between 10 and 20 (see eq 5) and Reynolds numbers between 90 and 220. The Froude number of a negatively buoyant jet is defined as:

$$\mathrm{Fr} = \frac{U_0}{\sqrt{R_0 \sigma}} \qquad 15$$

where R_0- is the nozzle radius, and $U_0$is the jet's velocity at the nozzle, defined as the ratio between the volume flow rate at the jet source and the nozzle cross-section, σ is the reduced gravity between the jet's fluid and the environment defined as $\sigma = g(\rho_0 - \rho_f)/\rho_f$, where ρ_0 is the mass density of the jet's fluid at the nozzle and ρ_f is the mass density of the fluid in the environment.

Tests were initially performed using high-speed camera flow visualization with external lighting and a jet dyed with acrylic paint. Each recording lasted 204 seconds at a rate of 24 fps, resulting in 4901 frames. For later simultaneous PIV and LIF measurements, three cameras and a double-cavity high-speed laser (Photonics DMX40-527-DH) were used. This laser has a pulse energy of 2 × 40 mJ at 1 kHz and a wavelength of 527 nm. The acquisition frequency for PIV and LIF recordings was set to 1.1 kHz. Camera

1 captured LIF measurements, while Cameras 2 and 3 were dedicated to planar PIV. Rhodamine 6G served as the fluorescent dye for LIF, and hollow glass spheres with a mean diameter of 10μm and a density of 1 g/cm³ were used for particle seeding. The data acquisition and processing were conducted using DaVis 10.2.1 software from LaVision GmbH. Planar PIV processing was applied to data from Cameras 1 and 2, with first-pass interrogation windows of 96 pixels and a 50% overlap, followed by second-pass interrogation windows of 48 pixels and an 87.5% overlap. The spatial resolution, without overlap, was 0.86 mm. Table 10 provides a summary of the experimental conditions for each case studied, including Froude (Fr) and Reynolds (Re) numbers, the relative density difference between the jet density and the environment density, defined as $\Delta\rho/\rho = (\rho_0 - \rho_f)/\rho_f$, and the jet's velocity at the nozzle U_0. All flow visualizations were performed using pure water as the surrounding fluid. For the initial three visualizations (FV1, FV2, and FV3 in Table 10), the jet fluid was a mixture of water, NaCl, and acrylic paint. In cases FV4 and FV5, a combination of water, glycerol, and acrylic dye was used.

Table 10: Text matrix of the experiments.

Exp. name	**Fr**	**Re**	$(\boldsymbol{\rho_0 - \rho_f})/\boldsymbol{\rho_f}$	$\boldsymbol{U_0}$, [m/s]
FV1	10	120	2.0	0.14
FV2	12	170	2.9	0.21
FV3	18	220	2.1	0.26
FV4	17	159	2.2	0.26
FV5	14	129	2.2	0.21
PL1	33	210	5.7	1.10

The results of the high-speed flow visualizations confirmed the observations of Williamson et al. (2008) regarding the unstable behaviour of fountains. In particular, we observed similar patterns of sinuous oscillation and jet breakdown, consistent with the instability mechanisms identified in their study. In Figure 26 (left), a jet oscillates above $\frac{y}{D} \simeq 35$, exhibiting sinuous instability. In Figure 26 (right), both sinuous oscillation and jet breakdown are visible in the region $20 \leq \frac{y}{D} \leq 38$. These instabilities occur due to the interaction between the descending fluid and the upward jet. The jet's height over time is characterized by an initial rise, followed by oscillations around a steady mean height. We determined the instantaneous jet height by analyzing the intensity gradient in the flow visualizations. The characteristic frequency of height variation over time was computed using the power spectral function. Figure 27 shows the power spectrum for flow visualization experiment FV2 as an example, where the peak of the spectrum provides the dominant frequency f . Multiple peaks were observed for each experiment, consistent with findings in previous studies by Burridge and Hunt (2016). To compare with past literature, results were plotted in a form of Strouhal number defined as:

$$\mathrm{Str} = f\frac{R_0}{U_0} \qquad 16$$

for the largest peak in the power spectrum for each experimental case against the corresponding Froude number (Figure 28). A good agreement is observed between the results of the present study and those of Williamson et al. (2008) and Burridge and Hunt (2016).

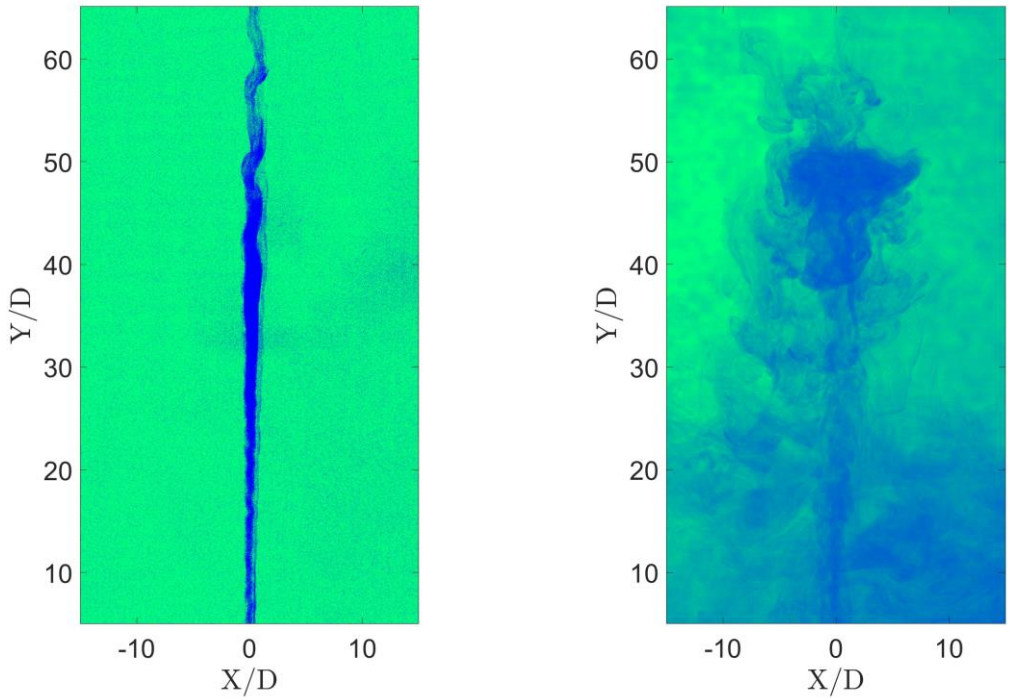

Figure 26: Flow visualizations. Test FV1 Fr = 10, Re = 120 (left); Test FV4 Fr = 17, Re = 159(right).

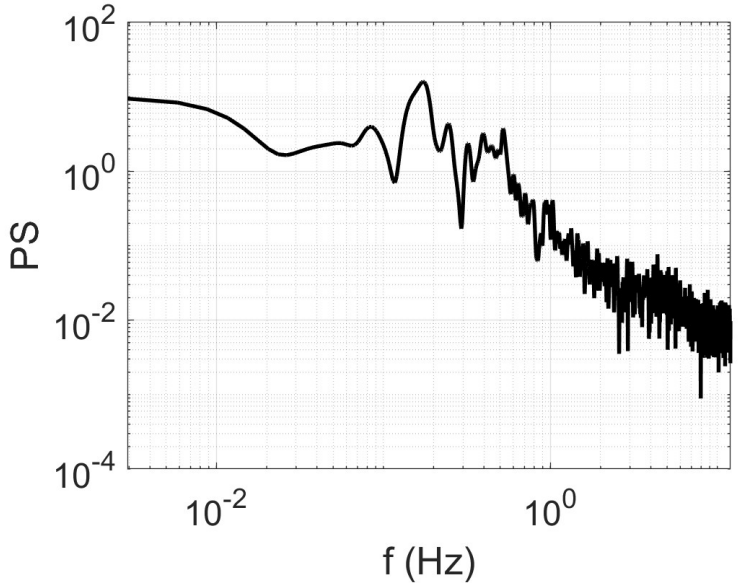

Figure 27: Power spectrum of experiment FV2 (Fr = 12,Re = 170).

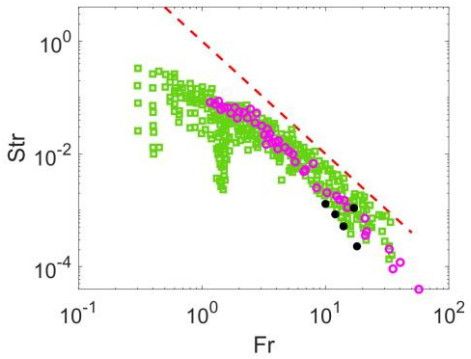

Figure 28: Strouhal number, (black dots) compared with data from Burridge and Hunt (2016) (green empty squares) and Williamson et al. (2008) (pink circles), versus the Froude number. The scaling $\sim Fr^{-2}$ is shown by the red dashed line.

The mean jet height after the initial rise is shown in Figure 29, along with data from Williamson et al. (2008) and a comparison with the scaling $\frac{H_m}{R_0} \sim FrRe^{0.5}$ proposed by Philippe et al. (2005). There is good agreement with Williamson's data within the same range of Froude and Reynolds numbers.

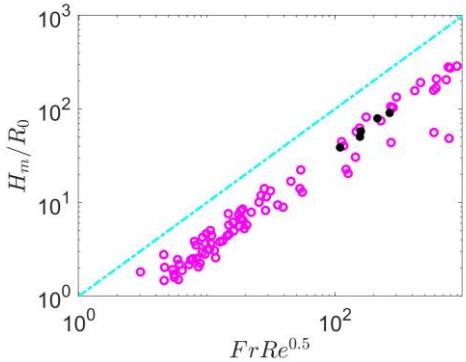

Figure 29: Time-averaged maximum jet's height (black dots) compared with data from Williamson et al. (2008) (pink circles), as a function of $FrRe^{0.5}$ as in the scaling of Philippe et al. (2005) (cyan line).

The collapse of a fountain at a Froude number $Fr = 33$and Reynolds number $Re = 210$ was captured using high-speed Particle Image Velocimetry (PIV) and simultaneous Laser-Induced Fluorescence (LIF) measurements. **Figure 30** (left column) displays four consecutive snapshots of the planar velocity fields during the fountain's collapse. Notably, the collapse of the fountain cap onto the up-flow jet causes it to split into two parts and expand horizontally. Interesting features include the two curls formed at the ends of the horizontal arms of the collapsing fountain, which oscillate vertically, as observed in a longer time series. The right column of **Figure 30** shows the out-of-plane vorticity component of the velocity fields on the left, calculated as follows:

$$\omega_z = \frac{\partial U_Y}{\partial x} - \frac{\partial U_X}{\partial y} \quad (17)$$

where: U_X and U_Y are instantaneous horizontal and vertical velocity components, respectively.

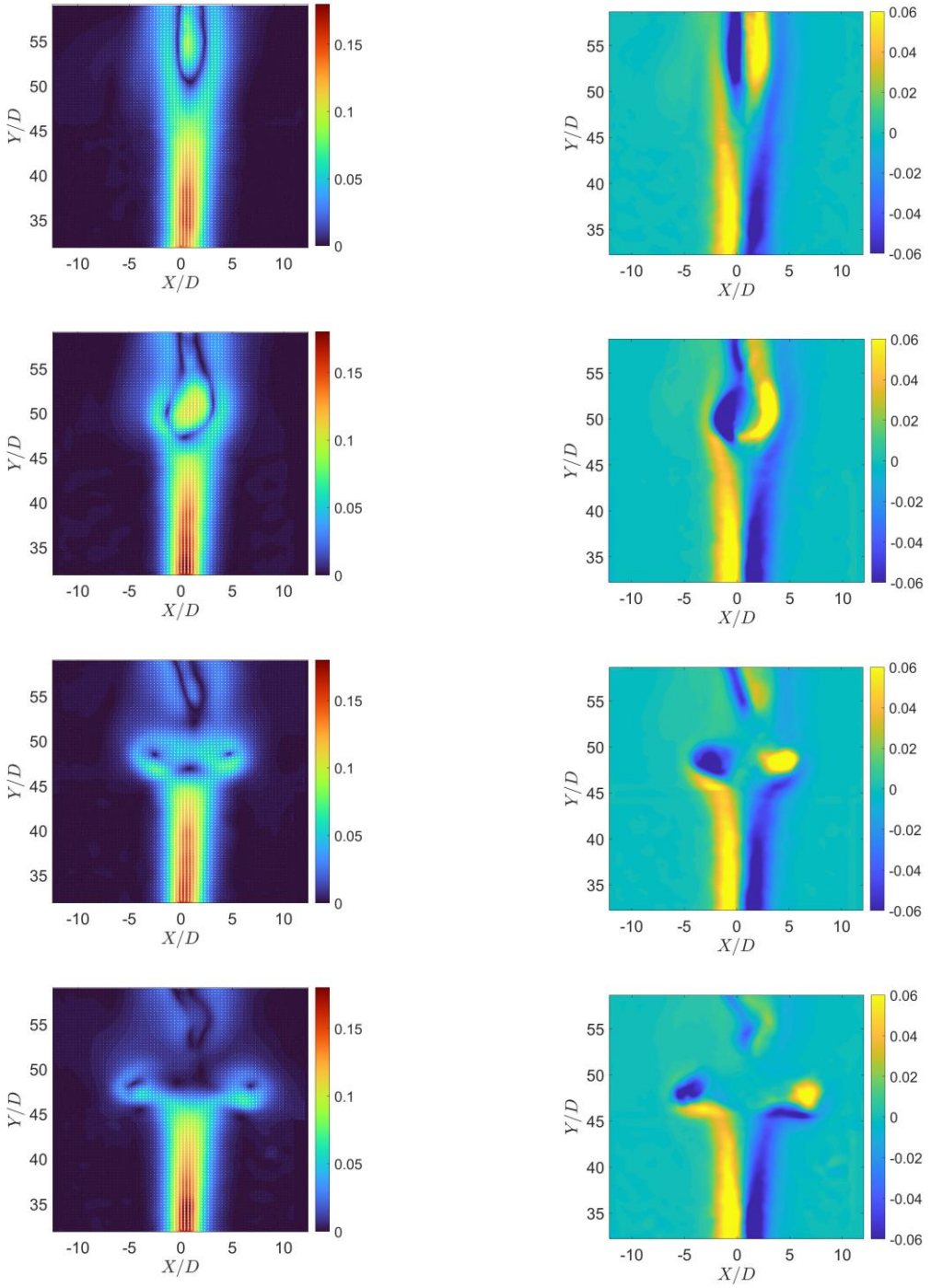

Figure 30: Contour plots of the instantaneous velocity magnitude in absolute value (left) and flow vorticity (right) at Fr = 33 and Re = 210 with 0.25 s time difference with the consecutive row.

Figure 31 (left column) presents the concentration fields obtained using the LIF technique simultaneously with the PIV measurements shown in Figure 30. The concentration fields reveal how the jet top collapses and then spreads horizontally, splitting into two parts with curls at the ends. By combining velocity and concentration fields over time, we quantified the mass flux coefficient between

the jet and the environment, a critical parameter for applications such as modelling pollutant dispersion in the atmosphere. The mass flux, MF, is defined as:

$$MF = \frac{(C_{t+\Delta t} - C_t) \times V}{A \times \Delta t} \quad 18$$

where $(C_{t+\Delta t} - C_t)$ is the concentration change between consecutive recording times, V is the volume of fluid crossing the interface between the jet and environment, A is the area of this interface, and Δt is the time interval. C_0 and C_f represent the concentration of the jet at the nozzle and the initial environmental concentration, respectively. In planar measurements, V is two-dimensional, and A is one-dimensional, with $V = A \times d$, where d is fluid displacement from PIV measurements.

$$M = \frac{MF}{(C_0 - C_f) \times U_0} \quad 19$$

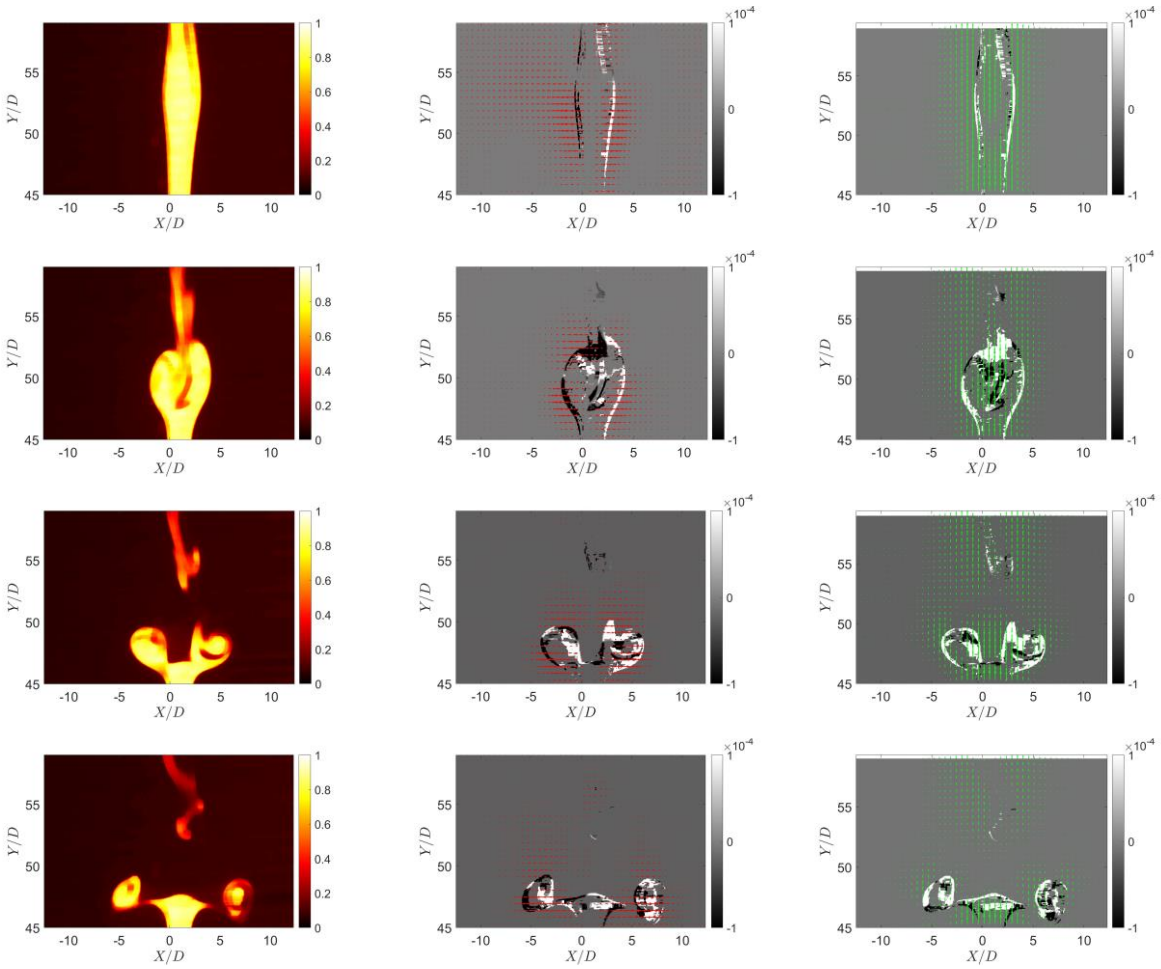

Figure 31: Contour plots display the concentration fields C (left), M_X(middle), M_Y(right). For Fr = 33 and Re = 210 (PL1) with 0.25s time difference with the consecutive row.

where: U_0 is the initial jet velocity. Additionally, the mass flux coefficients in the horizontal (M_X) and vertical (M_Y) directions are defined as:

$$M_{X,(Y)} = \frac{(C_{t+\Delta t} - C_t)}{(C_0 - C_f)} \times \frac{U_{X,(Y)}}{U_0} \quad 20$$

The snapshots of mass flux coefficients in Figure 31 highlight that most mass exchange occurs at the cap and edges of the fountain. The concentration difference, ΔC is concentrated at the jet borders for small Δt(e.g., 0.25 s), indicating localized mass exchange in these regions.

The novel high-resolution experimental database discussed in this chapter will be used in the future for the further development and validation of CFD models, to be used for the prediction of thermal stratification in LMFR pools.

3 Task 2: occurrence of hot spots on LMFR fuel cladding in the presence of wire-wrap

3.1 Experimental Facility: Wire-wrap test section

The wire-wrap facility is aimed at investigating the occurrence of hot spots on the fuel cladding of a liquid-metal cooled fast reactor, due to the presence of a wire-wrap. Wire-wraps are used in the fuel assemblies of liquid metal cooled reactors to ensure that neighboring fuel rods do not come into contact with each other. Because the wire-wrap are made of stainless steel, which has a lower thermal conductivity than liquid metals used as coolant in fast reactors, the wire-wrap introduces an additional thermal resistance between the fuel cladding and the coolant itself, leading to the potential occurrence of hot spots at the locations of the fuel cladding where the wire-wrap is soldered.

The wire-wrap experimental facility designed for this project uses GalInStan as liquid metal operating fluid. This because GalInStan is already liquid at ambient temperature and does not react with water or air, like liquid sodium. Therefore, GalInStan is much simpler to handle in a laboratory setting.

The facility (see Figure 32) consists of a heater, a wire soldered on a surface to simulate a fuel cladding wall with wire-wrap, a cooling element, insulation to limit heat losses and a sapphire window to be able to measure high-resolution temperature distribution on the cladding wall using an infrared (IR) camera.

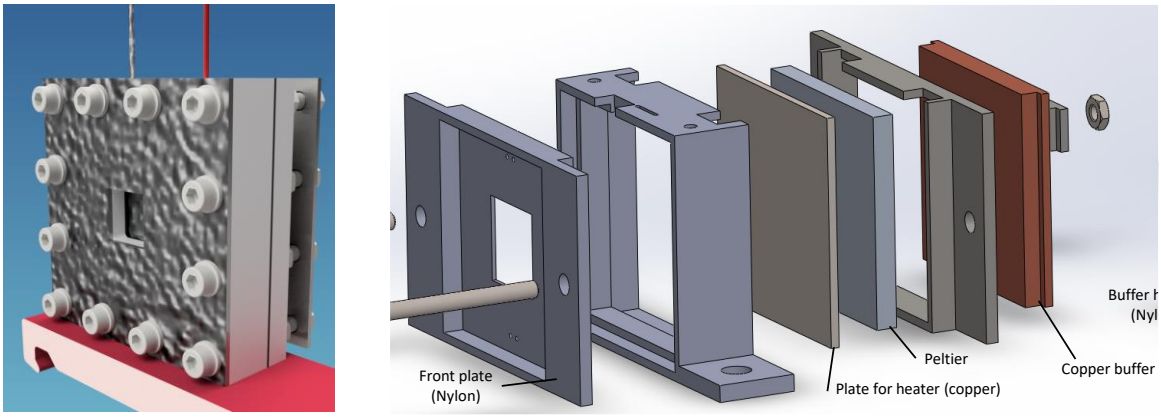

Figure 32: Illustration of the wire-wrap setup (left) and CAD of mock-up details (right)

The facility has been designed taking into consideration good thermal insulation, maintainability and chemical resistance of the applied materials. The selection of materials for the experimental facility is of special importance, as Geddis et al. (2020) have proved that Nylon echibits strong corrosion in contact with GalInStan, while a negligible effect was found for PTFE (Teflon). Therefore, the setup enclosure is manufactured from PTFE (Teflon), which has very high chemical resistance to almost every chemical. The material thickness of the thinnest part is 8 mm and could be increased with another PTFE plate up to 28 mm to increase the thermal insulation of the overall enclosure. The sealing is provided with silicone gaskets, and the sapphire window is fixed with stainless steel clamps against a gasket in the enclosure. The wire, placed in front of the sapphire window is laser welded on two of the clamps. This enables the opportunity to give some pre-tension on the wire to push against the stainless steel foil, placed between the wire and the sapphire window. To avoid reflections of the stainless steel foil, a black paint is sprayed on the outer surface of the foil. The same approach is used for the front plate, which holds the mockup together. The setup has been designed such that the depth of the cavity can be adjusted by changing the inner distance holder of the enclosure. A stainless steel plate is used to transport the heat from a

Peltier element to the cavity with the liquid metal inside. On the back side of the Peltier element, a copper plate with a ventilator mounted on its backside is used to enhance the efficiency of the Peltier element. Finally feed through holes from the top and the bottom are used to fill and drain the cavity and to feed through measurement devices, such as thermocouples.

3.2 Results and discussion

3.2.1 Experimental results

Liquid metal-cooled fast reactor (LMFR) designs typically use helically wire-wrapped pin bundles to prevent direct contact between adjacent fuel rods. However, the lower thermal conductivity of the wire wrap compared to liquid metal coolants (e.g., sodium) introduces additional thermal resistance between the fuel cladding and the coolant. This resistance can lead to potential hot spots beneath the wire wrap. The wire-wrap facility was designed to investigate the occurrence and severity of such hot spots on the fuel cladding of an LMFR. Figure 33 shows the test section assembly, which includes heating elements, a wire on a surface to simulate a fuel cladding wall, and a sapphire window for high-resolution wall temperature measurement using an infrared (IR) camera. The internal volume of the test section (50 x 50 x 6 mm³) was filled with heat transfer fluid. An infrared camera (FLIR-SC7000) captured the temperature distribution along the inner wall in contact with the wire. A 1 mm-thick sapphire window in the measurement section enabled effective transmission of mid-wave infrared radiation for thermography. To generate heat flux through the sapphire wall, the internal fluid was heated with a heater on the backside of the test section. The sapphire surface was cooled by air injected at -13°C using a vortex tube. To minimize heat loss from surrounding convection, a 3D-printed wind shield with four nozzles was installed to supply air evenly around the measurement area. This setup effectively generated and quantified high heat flux in an IR thermography experiment. However, the heat flux on the wire and measurement surface was oriented opposite to the actual heat transfer in a fuel rod bundle. Based on postulated similarity, the negative peak in wall temperature observed in this experiment was interpreted as a hot spot within the fuel rod.

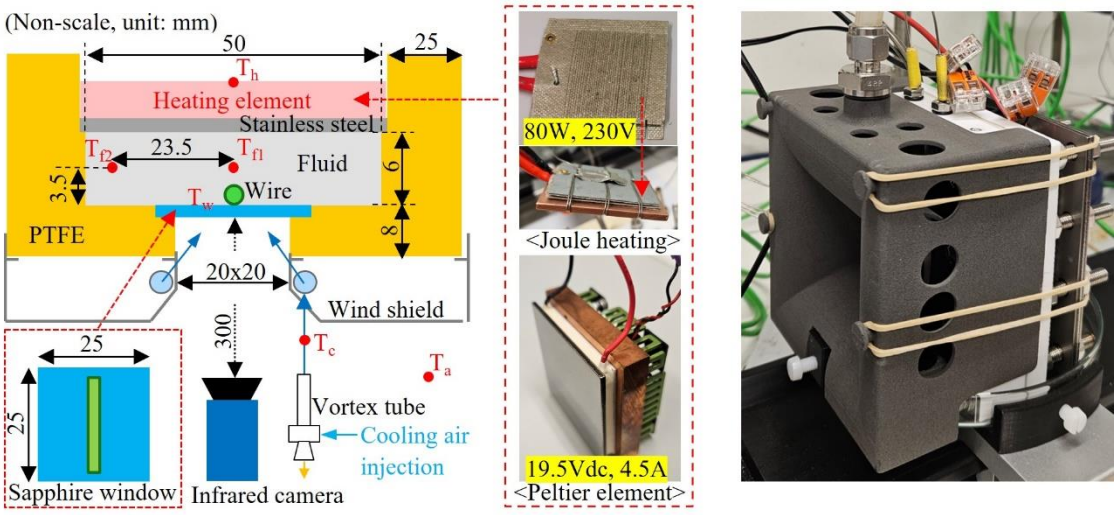

Figure 33: Schematic diagram and assembly of the test section

A liquid metal Galinstan was used to simulate a low Prandtl number (Pr) coolant in the LMFR. Galinstan is a commercially available liquid metal alloy consisting of gallium, indium, and tin (69:22:9 % of wt.). It has the advantage of being stable liquid at room temperature, low toxicity and reactivity. Table 11 shows the thermal properties of low Prandtl number liquid metals, as well as water and silicone oil, which were also used to investigate the influence of fluid properties.

Table 11: Thermodynamic properties of working fluids

Fluid properties	Working fluids				
	Sodium (400℃)	Lead (400℃)	Galinstan	Water (24℃)	Silicone oil (350cSt) (25℃)
Expansion coefficient (cc/cc/K)	2.0×10^{-4}	8.4×10^{-5}	1.26×10^{-4}	2.58×10^{-4}	1.07E-3
Density (kg/m^3)	856	10580	6440	997	968
Dynamic viscosity (Pa-s)	2.8×10^{-4}	2.2×10^{-3}	2.4×10^{-3}	8.88×10^{-4}	0.339
Specific heat (J/Kg-K)	1282	147	296	4181	1600
Thermal conductivity (W/m-K)	72.4	16.6	16.5	0.607	0.142
Prandtl number, Pr (-)	0.005	0.0195	0.043	1.98	3817

In the subchannel condition of sodium fast reactor (SFR), thermal conductivity of sodium is much greater than that of the wire and cladding material. However, the Prandtl number of Galinstan is not as low as that of sodium of the typical operating temperature in the SFR. Particularly, the thermal conductivity of Galinstan is very similar to that of the stainless steel (SS) which was used to simulate the wire and fuel cladding in the present tests. As alternative material of the low thermal conductivity, the other wires made of zirconium oxide (ZrO_2) and polymer of methyl methacrylate (PMMA) were also considered along with the geometry effect from different wire sizes and shapes, as listed in Table 12. Figure 34 shows different wire specimens for each test case and the detailed schematics of each different cross-sectional shape to investigate the influence of geometry and physical properties of the material. Each wire was firmly fixed on the inner surface of the sapphire glass.

Table 12: Test cases with different wire configurations and properties

Case	Material	Shape	Height (mm)	Contact area	Density (kg/m^3)	Specific heat (J/Kg-K)	Thermal conductivity (W/m-K)
-	Sapphire	-	-	-	3970	757	40
T1	SS	Circle	1.6	Point	7930	490	16.3
T2	ZrO_2				5680	480	1.7
T3	PMMA*				1170	1466	0.19
T4			2.5				
T5			2.0				
T6		Key hole		1 mm width			
T7		Horseshoe		2 mm width			

* Made with 3D printing to investigate the effects of different shapes and contact area.

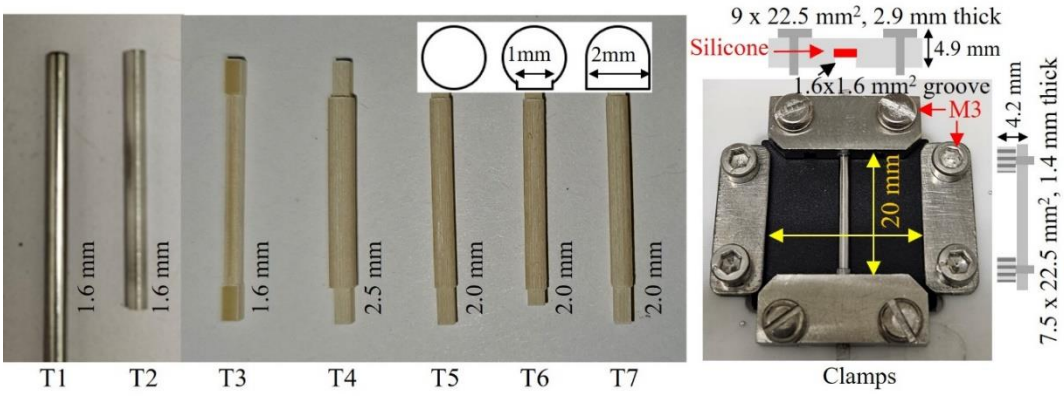

Figure 34: Different wire specimens and schematics of the cross-sectional shape

The heat flux through the sapphire window of the test section was calculated as follows.

$$q" = h(T_{f1} - T_w) \qquad 21$$

T_{f1} is the fluid temperature measured at the center of the test section, and T_w is the wall temperature distribution of the inner surface measured with the infrared thermography. This method provides heat flux distribution in nearly real-time, and a quasi-steady state condition can be easily achieved at the desired heat flux without having to consider heat losses through the test section structure.
To determine the heat transfer coefficient required in the equation above, a characteristic test was conducted under various steady state heat flux conditions using joule heating method without the wire in the test section. Under steady-state conditions, the average heat flux and heat transfer coefficient was measured from the input power of the Joule heating element and the heat loss function indicated in Figure 35a. Based on the characteristic test data, a correlations for the natural convection heat transfer coefficient with Rayleigh number (Ra) and Nusselt number (Nu), and the empirical coefficients were derived as shown in Figure 35b according to the fluids, as follows:

$$Nu_L = \frac{hL}{k_f} = C_0 + C_1 Ra^{C_2} \qquad 22$$

$C_0 = -46.0$, $C_1 = 24.3$, $C_2 = 0.0842$ for Galinstan
$C_0 = -32.2$, $C_1 = 1.83$, $C_2 = 0.252$ for water
$C_0 = -59.1$, $C_1 = 0.83$, $C_2 = 0.438$ for silicone oil

Here, the characteristic length L in Nusselt number is 0.02 m, which is the vertical length of the heat transfer area, k_f is the thermal conductivity of the fluid, and Rayleigh number represents the ratio of buoyancy and thermal diffusivity. The heat flux measurement method in the present study provides the local distribution with high data productivity, along with the use of the Peltier element which can easily control the electric power and temperature.

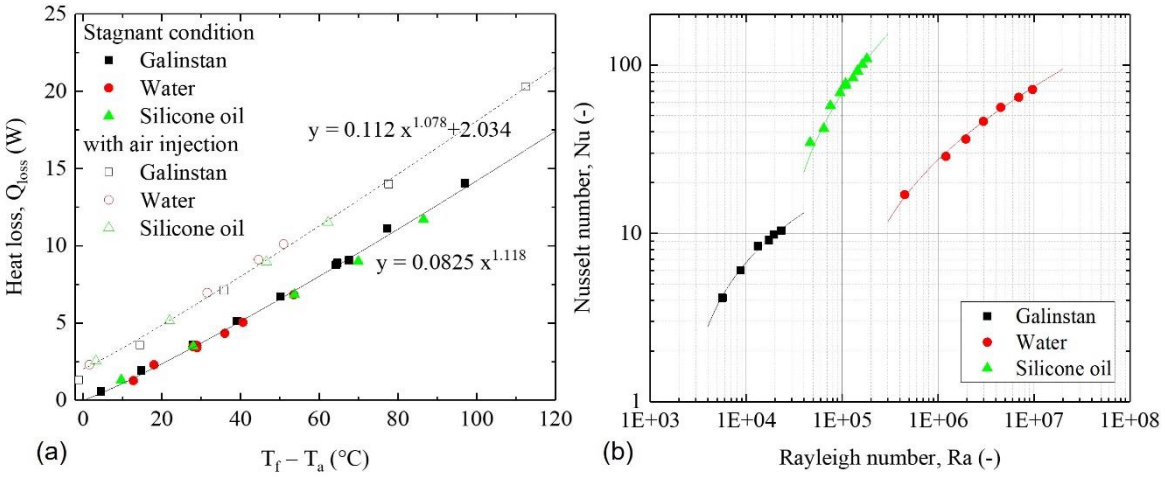

Figure 35: Characteristics of the test section: (a) heat loss with respect to the fluid temperature and (b) natural convection heat transfer coefficient.

An infrared camera (FLIR_SC7000) was used to measure the inner wall temperature of the test section. A sapphire glass was used for high transmittance in mid-wave infrared band and internal wall was painted to efficiently measure the internal wall regardless of fluid type. Figure 36 shows an example data of the internal wall temperature distribution (T_w) measured under Galinstan conditions with 1.6 mm diameter circular PMMA wire. The image represents an area of 20 x 20 mm^2 with pixel resolution of 0.16 mm/pixel. The temperature peak $\Delta T_{w.peak}$ was defined as the difference between the wall temperature at the wire contact point and the surrounding wall temperature which was not affected by the wire. In the present tests, uneven distribution of the heat flux and wall temperature appeared due to the nature of the air injection cooling method. The background wall temperature distribution was reconstructed as polynomial fitting curves for the temperature profile excluding the wire contact region. Distribution of the temperature peaks obtained by subtracting the background T_w from the measured T_w. In all data sets, the heat flux peaks consistently appeared 4.5 mm below the center point due to the asymmetric nature of the air injection, thereby local heat flux and hot spot were consistently analyzed at this peak region to minimize the measurement uncertainty caused by the heat flux gradient.

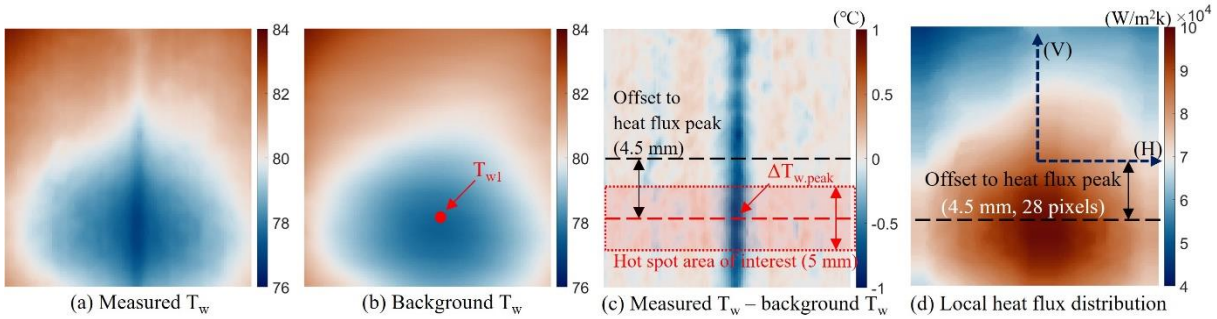

Figure 36: Infrared thermography images of the wall temperature distribution and image processing scheme for the local T_w peak and heat flux distribution

Figure 37a shows the wall temperature peak distribution corresponding to the indicated red area in Figure 36c. The example data were measured under various heat flux conditions with Galinstan and ZrO_2 wire of 1.6 mm diameter. The negative peak of the wall temperature corresponds to the hot spot

occurring in the actual fuel rod clad considering the heat flux direction. The temperature peak was observed at the wire contact point and the peak becomes larger as the heat flux increases. Figure 37b shows that the extent of the hot spot is linearly correlated with the local heat flux and it is independent of the fluid temperature from the data obtained under various cooling conditions.

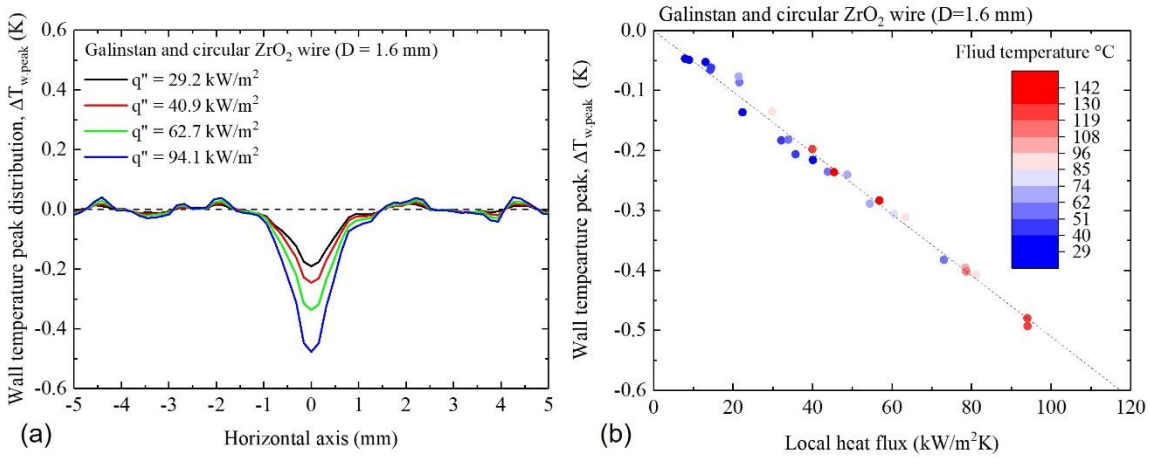

Figure 37: (a) Wall temperature peak profiles and (b) linear relationship with the local heat flux

The influences of the material properties and size of the wires were investigated from various wire configurations. Figure 38 shows the wall temperature peak for various test conditions. In the case of Galinstan conditions, the negative peaks always appeared due to low thermal conductivities of the wire material compared to that of the fluid and. With the stainless steel wire which has similar thermal conductivity to Galinstan, the hot spot was very small, less than 0.1℃. For the PMMA wires, which has the lowest thermal conductivity, the largest hot spot occurred, and it increased with increasing the diameter. With non-metallic fluids of water and silicone oil, positive temperature peaks were observed with the ZrO_2 wire, which have higher thermal conductivity than that of the fluids. In these cases, the temperature gradient inside the wire is small and the heat transfer is mainly determined by the thermal resistance of at the fluid/surface boundary, so additional heat transfer area by the wire surface enhances the heat transfer, which is considered as fin effect. Under such cases, slightly nonlinear relationships of the temperature peak arise from the complexity of convective heat transfer. Despite the large difference in thermal conductivity of between stainless steel and ZrO_2, there was no significant difference in the temperature peak. Under the conditions where the fin effect appears, the temperature gradient inside the wire is more likely uniform, and thus the thermal conductivity of the object has a relatively small influence on local thermal resistance.

In the case of silicone oil, even though the thermal conductivity of PMMA wire was slightly higher than that of silicone oil ($k_w > k_f$), hot spots still occurred rather than the fin effects. The non-metallic fluids usually have higher Nusselt number than that of liquid metal. This means that the conductive thermal resistance offered by the interior of the wire exceed that of convection at fluid/surface boundary, causing the internal temperature gradient and a local hot spot at the wire contact location. That is, the Nusselt number plays an important role along with the thermal conductivity ratio on the temperature distribution. To determine the likelihood of hot spot formation, the Biot number was defined as a criterion, indicating the influence of convective heat transfer around a conducting body which can be estimated as follow:

$$Bi = Nu\frac{1}{4}\frac{k_f}{k_w} = \frac{hD}{4k_w} \qquad 23$$

In Biot number, characteristic length was defined as the volume of the wire body divided by the surface area, which corresponds to the quarter of the wire diameter, while the characteristic length in Nusselt number was the outer diameter of the wire. It is noted that Biot number consist of thermal conductivity of wire material, while Nusselt number consist of thermal conductivity of fluid. The present results showed that the Biot number was always greater than one for the conditions where the hot spots occurred.

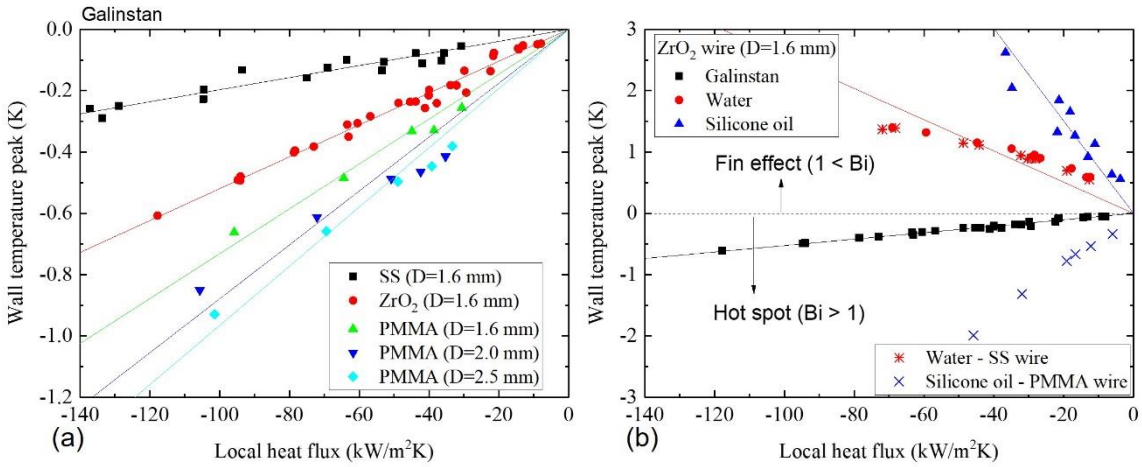

Figure 38: Effects of parameters on the hot spot wall temperature peak: (a) wire material and size and (b) fluid property

The influence of contact area and wire geometry on the temperature peak was investigated by using different wire cross-sectional shape. Figure 39 illustrates the temperature peak distribution corresponding to the contact area of different PMMA wires in Galinstan conditions. As increased in both contact area and wire volume increased, the effective area of the hot spot and temperature peak increased, attributed to a large internal temperature gradient at the contact point and restricted convection by fluid access. These findings suggest that minimizing the contact area of the wire and improving fluid access beneath the wire may help mitigate hot spots.

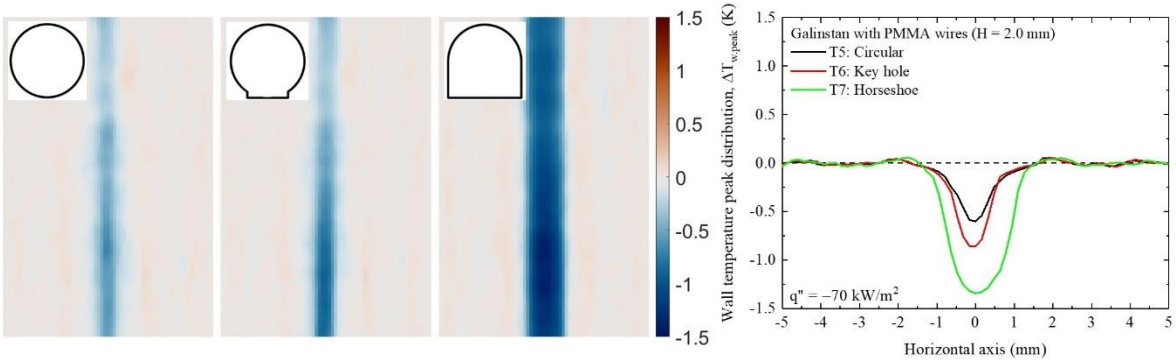

Figure 39: Effect of volume and contact area of wire cross-section on the hot spot wall temperature peak

3.2.2 CFD simulation results

A preliminary set of CFD simulations (using STAR CCM+) was conducted on a wire wrap facility to examine the detailed effects of wire parameters and to assess the impact of forced convection under

flow conditions extending beyond previous experimental settings. For simplification, the model simulated a 20 x 20 mm² heat transfer area with a 6 mm fluid volume and a 1 mm sapphire wall, as shown in Figure 40. A uniform heat flux (10-100 kW/m^2) was applied to the fluid wall, while convection conditions (T_a = -13C, h = 600 W/m^{2}K) were applied to the outer window wall, respectively, consistent with experimental setting.

Figure 41 shows the sensitivity of the mesh size on the wall temperature peak, revealing insignificant impact when the base size is below 1 mm. For the grid continuity, the wire requires a minimum shared volume with the wall. In modeling the contact region, an increase in overlap thickness correspondingly raises the temperature peak. This analysis was performed under various conditions such as stagnant and flow condition (using a turbulence model), and the results consistently showed that the offset distance have minimal impact in the simulation, Besides, no significant discontinuity was observed even in non-contact conditions. Based on the sensitivity analysis, the wire was designed with 0.01 mm onto the sapphire window, using polyhedral meshes with a base size of 1 mm and 20% of the base size for a surface control at the fluid contact area and wire volume.

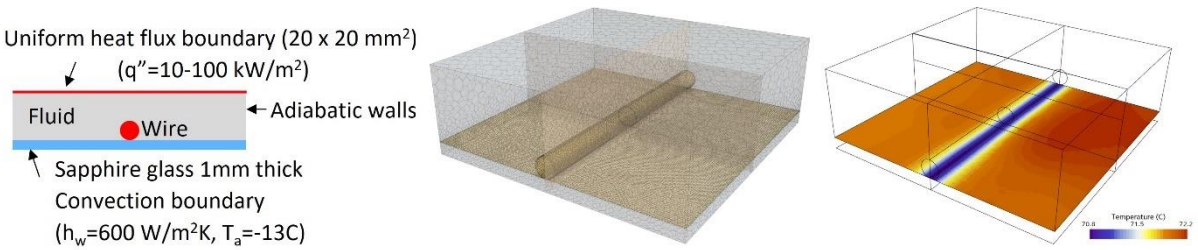

Figure 40: CFD simulation model for the hot spot measurement test section

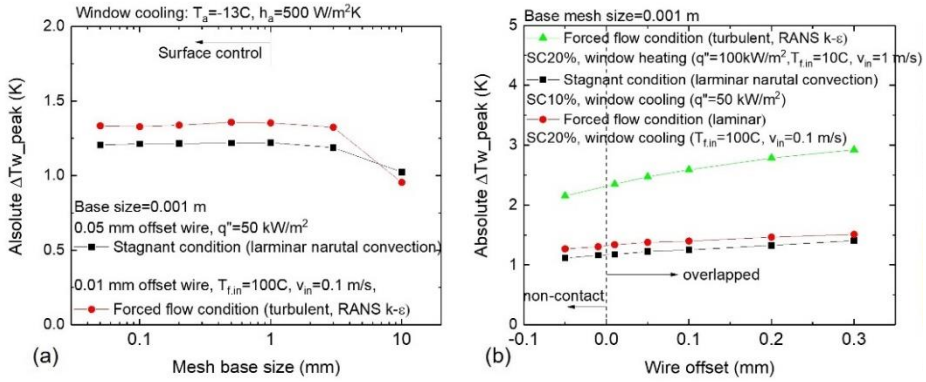

Figure 41: Sensitivity of mesh size and wire contact model

Figure 42 shows typical simulation results from various heat transfer models: (a) liquid conduction only, (b) a stagnant condition modelling the experimental condition under natural convection (using the Boussinesq Model), and (c) a flow condition (turbulence model: k-ε) with a uniform heat flux applied to the window. for the flow condition, a fully developed velocity distribution was applied by incorporating an upstream grid extension of 10D (100 mm) and a downstream extension of 1D (10 mm). The window cooling condition (a,b) corresponding to the experimental conditions produced a negative heat flux and T_w peak, while wall heating condition (c) shows positive T_w peak, which is similar to the wire-wrapped bundle condition in an actual SFR. The T_w peak at the wire contact point was determined from the wall temperature profile along the horizontal centerline, consistent with the data processing method used in the experiments. Figure 43 compares the linear relationship of T_w peak across different heat transfer

models. Simulations conducted under identical material and geometric parameters show a consistent linear correlation with the heat flux, indicating that the hot spot is primarily dominated by heat flux regardless of the heat transfer method applied. This finding validates the experimental assumption of the similarity in the heat transfer direction, as both wall heating and cooling conditions align with the same linear relationship.

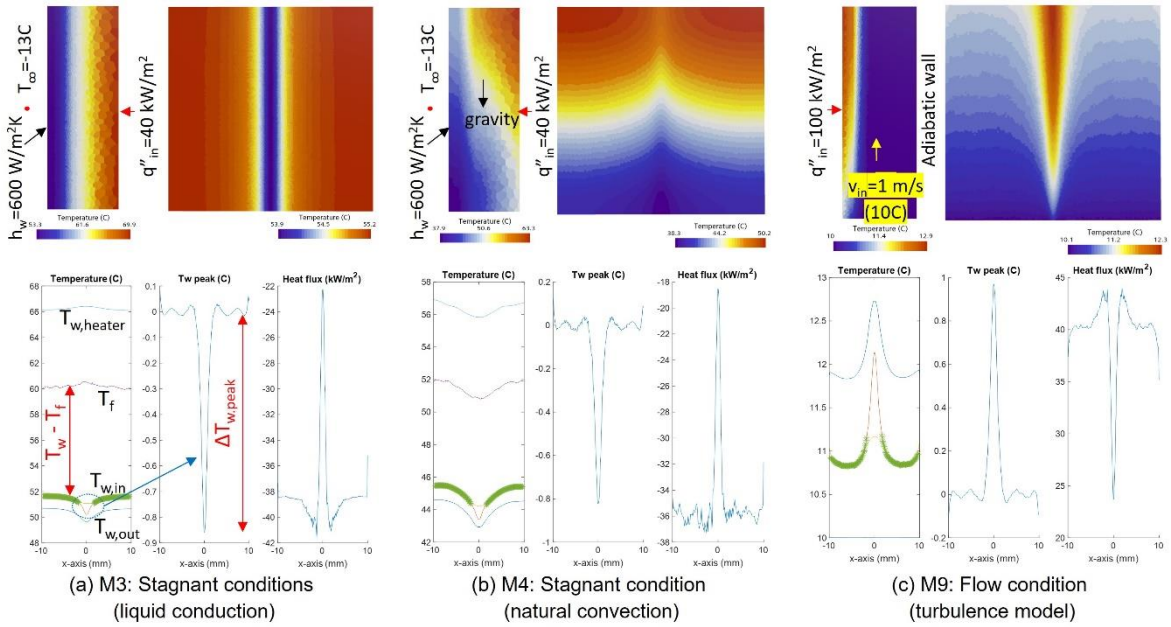

Figure 42: Wall temperature distribution of the CFD simulation and hot spot data reduction (galinstan with 1.6 mm PMMA wire, q"=40 kW/m²)

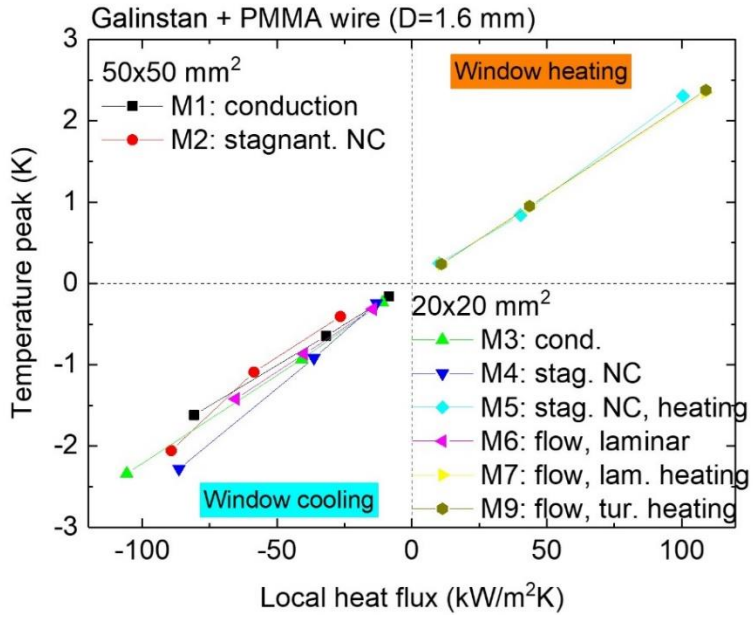

Figure 43: Dependency of hot spot Tw peak on the local heat flux for various heat transfer configurations

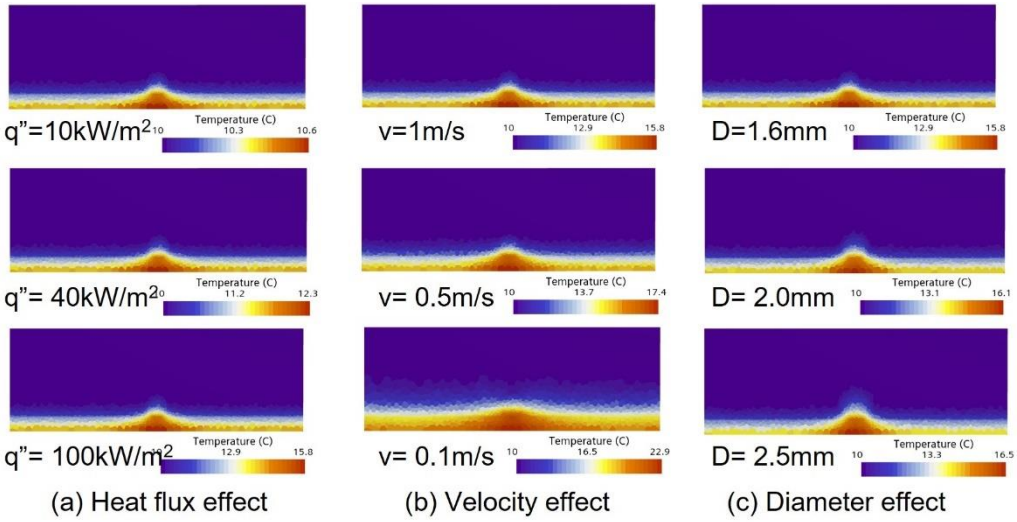

Figure 44: Effects of key parameters on the temperature distribution under forced convection conditions with control variables: q"=100 kW/m^2 , v=1 m/s, D=1.6 mm

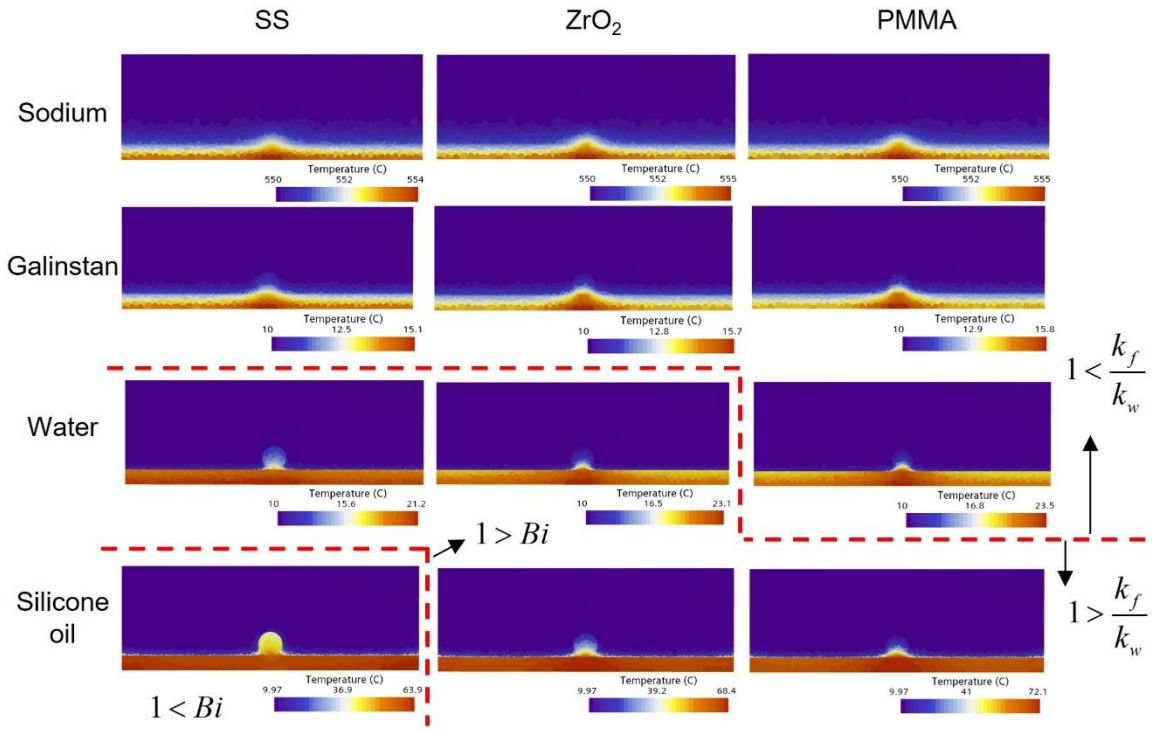

Figure 45: Effects of material properties on the temperature distribution under forced convection, with control variables: q"=100 kW/m^2, v=1 m/s, D=1.6 mm

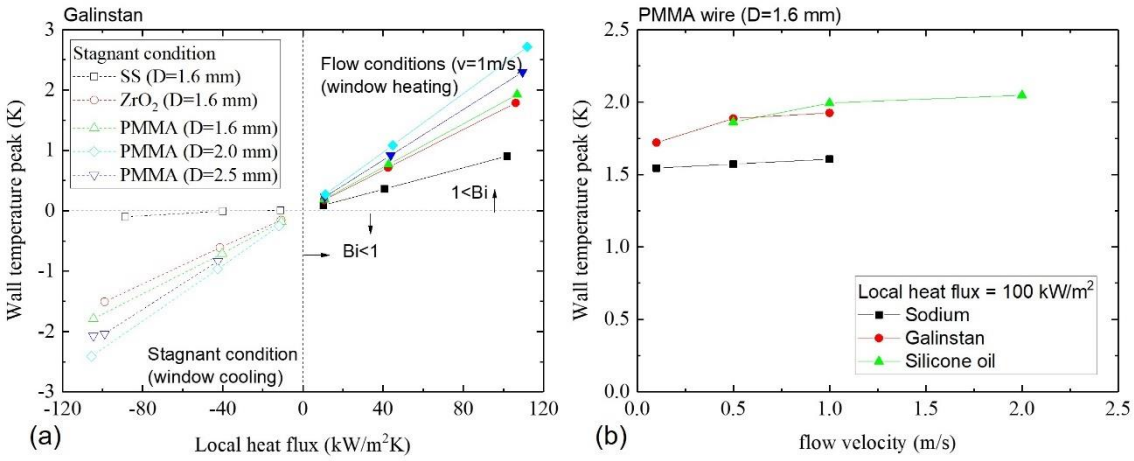

Figure 46: Effects of parameters on peak hot spot wall temperature: (a) wire material and size, and (b) flow velocity

Figure 44 and Figure 45 show simulated wall temperature distribution under different flow conditions. Hot spots were observed across nearly all test scenarios, except for a one case involving silicone oil and stainless steel wire, where Biot numbers remained below unity under the given forced convection conditions. Figure 46 shows the hot spot characteristics under both stagnant and flow conditions, showing symmetry trends for the T_w peak due to opposing heat flux directions along the wall. In stagnant conditions, the SS wire produced negligible hot spots due to a Biot number close to 1, In flow conditions, the Biot number rose, loading to a substantial increase in T_w peak compared to stagnant conditions. This finding highlights the Biot number is an important variable that determines the hot spot. Figure 46b reveals a slight increase in Tw peak with rising velocity under given flow conditions.

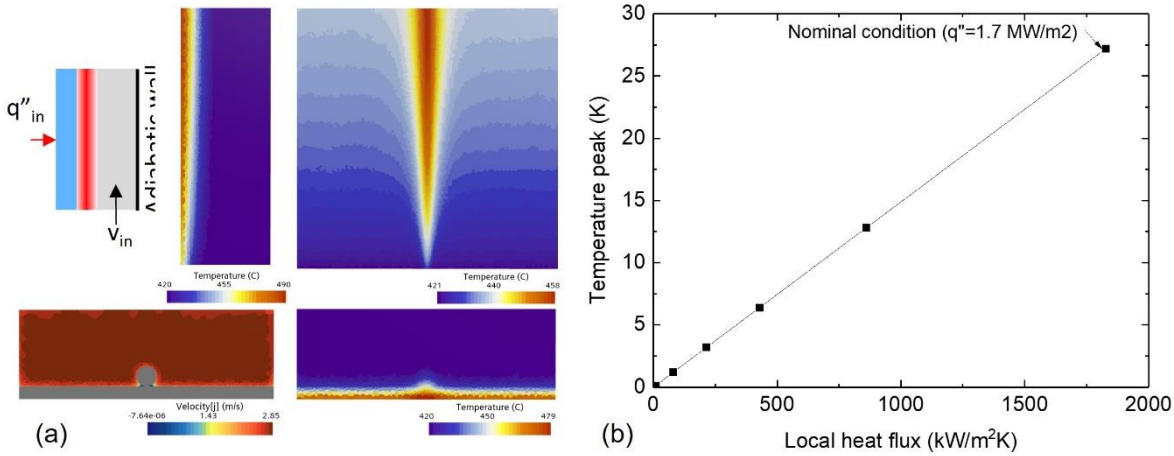

Figure 47: Hot spot simulation under nominal condition of SFR bundle

To predict the hot spot within the wire-wrapped pin bundle of an operational SFR, a simulation was performed under sodium conditions using the established CFD model. The wire with a diameter of 1.6 mm and the wall were modeled as stainless steel, while the nominal operating conditions were set to an inlet velocity of 2.8 m/s (Re: 94,200), an inlet fluid temperature of 420C, and the wall heat flux of 1.7 MW/m^2. Figure 47 presents the temperature and velocity distributions under forced convection, utilizing a RANS (k-ε) turbulence model. The peak wall temperature linearly increases with respect to the wall heat flux, with an estimated temperature peak of approximately 27 degrees at the nominal heat flux of

1.7 MW/m^2. The selection of the window wall material did not have a significant effect on the hot spot simulations.

3.2.3 Empirical correlation for hotspot wall peak temperature.

Figure 48 presents a schematic of a thermal circuit model, illustrating conduction at the wire contact point and convective heat transfer to the surroundings. When the Biot number exceeds unity, the thermal network modeling becomes more challenging, as it must account for non-uniform temperature fields within complex geometries accompanied by surrounding convection. To address these complexities, empirical correlations were developed to quantify hot spot intensity, based on the present experimental and CFD-generate data. The Biot number was used as a key non-dimensional parameter, serving as both a criterion for hot spot occurrence and an indicator of internal temperature gradient. To consider the convection effect at the wire surface, the Nusselt number was also incorporated. The hot spot intensity, represented by the wall temperature peak $\Delta T_{w.peak}$ was non-dimensionalized by the temperature difference between the surface temperature (background T_{w1}) and the bulk fluid (T_{f1}). The empirical correlations derived from this analysis are detailed in Figure 49 and their coefficients are listed as follows:

$$\frac{\Delta T_{w.peak}}{T_{w1}-T_f} = a(Bi-1)^b Nu^c Pr^d \text{ for Bi} > 1 \qquad 24$$

$$\text{where, } Bi = \frac{hD}{4k_w},\ Nu = \frac{hD}{k_f}\ Pr = \frac{c_p \mu}{k_f}$$

For the stagnant condition (based on the experimental data):

a=0.013; b=0.09; c=0.42; d=-0.45 (adj. R^2 = 0.959)

For the flow condition (based on the CFD-generated data):

a=0.106; b=0.007; c=0.43; d=-0.32 (adj. R^2 = 0.947)

Here, the Prandtl number was applied to account for variations in fluid properties affecting heat transfer and flow characteristics. Data obtained under silicone oil conditions exhibited large measurement uncertainty due to steep fluid temperature gradient. It is noted that the empirical correlation presented in Figure 49a exhibits a predictability in sodium conditions of CFD results. Although this correlation may have limited general applicability due to the simplified test setup, it offers valuable insights into wire wrap design considerations.

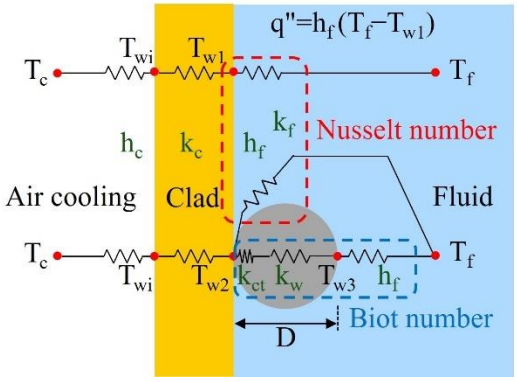

Figure 48: Thermal circuit model schematic around wire contact area

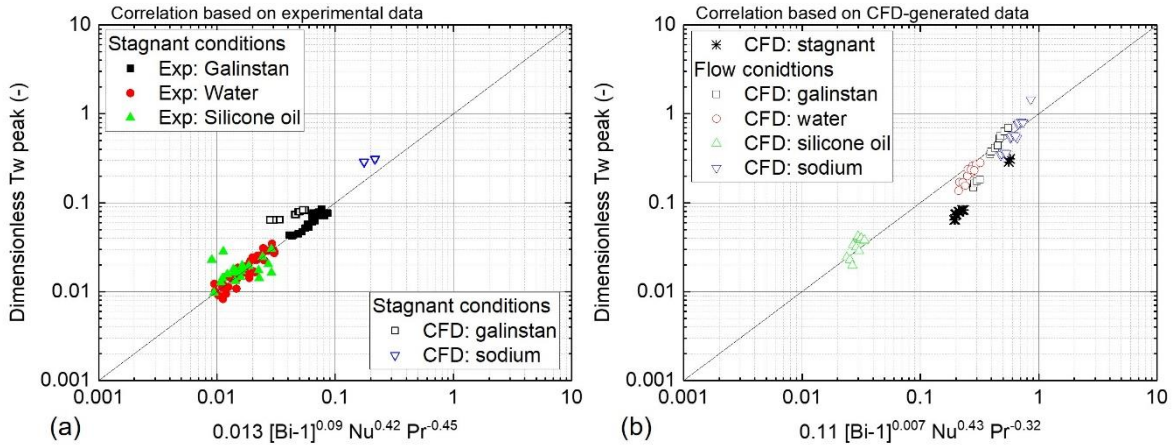

Figure 49: Empirical correlations for wall temperature peak from hot spots based on (a) experimental data for stagnant conditions and (b) CFD-generated data under flow conditions

3.3 Fuel bundle experimental facility

3.3.1 Hexagonal Bundle Layout

A test section layout was selected for the experiments of flow distribution and heat transfer within a wire-wrapped fuel bundle. Figure 50 shows the schematic and geometric parameters of the selected bundle layout. The pin is made of a transparent PMMA tube with an outer diameter of 15 mm (1 mm of thickness) and the pins are wrapped with wires of 2.85 mm of diameter at a pitch of 450 mm. The bundle lattice consists of up to 37 pins, and also compatible with 7 and 19 pin layouts.

Number of rods	7	19	37
Number of rods CTC	3	5	7
Number of side rods	2	3	4
CTC distance (mm)	61	97	133
FTF distance (mm)	53	84	115
area flow channel (mm²)	2'417	6'111	11'489
rod diameter D (mm)	15	15	15
Wire diameter D_w (mm)	2.85	2.85	2.85
rod pitch P (mm)	17.85	17.85	17.85
P/D	1.19	1.19	1.19
Wire pitch H (mm)	450	450	450
H/D	30	30	30
edge pitch W (mm)	18.31	18.31	18.31
rod length L (mm)	2'000	2'000	2'000
flow area (mm²)	1'135	2'632	4'713
wetted perimeter(mm)	576	1'357	2'475
Hydraulic Ø dh	7.88	7.76	7.62
Re	259-34'600	248-33'500	251-32'700
Q (m³/h)	0.12-16	0.27-36.5	0.5-65
j (m/s)	0.029-3.92	0.029-3.85	0.029-3.83
Δp (mbar)	0.35-504	0.35-499	0.38-604

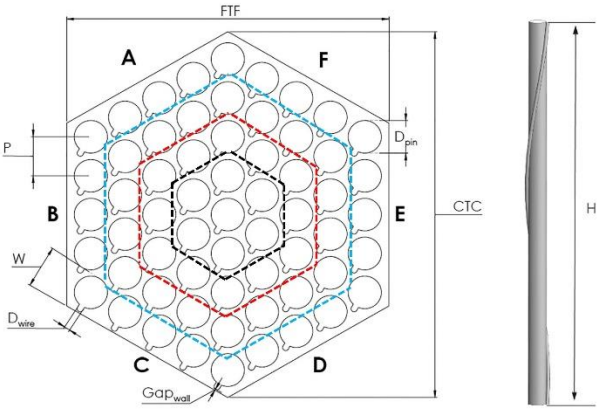

Figure 50: Summary of geometric parameters and schematics of the wire-wrapped bundle layouts with 7, 19, and 37 pins.

3.3.2 Facility construction and deviation from initial plan

The test section was planned for installation in the existing SUBFLOW loop (Ylonen, 2013). Figure 51 shows the pipe diagram of SUBFLOW and marks the modification plans for the bundle experiments. For the diabatic tests, a hot water loop was newly designed for each individual bundle pin. From a preliminary

analysis, about 25 kW of heat can be transferred to the subchannel of 30℃ through 37 pins at a hot water flow rate of 1.5 kg/s at 60℃, and the maximum heater power was determined at 40 kW. Additionally, a plate-type heat exchanger is installed in the main flow loop to maintain the temperature of the subchannel loop, using 30°C cooling water supplied from the building chilled water system.

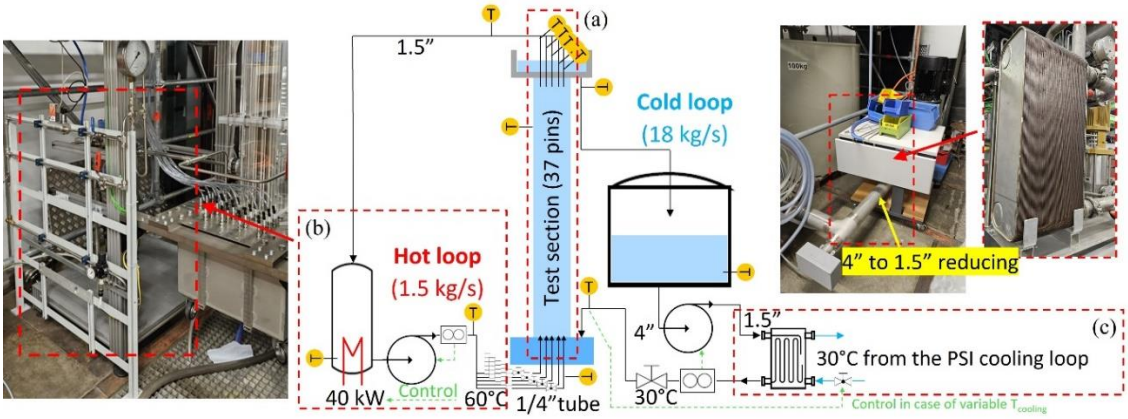

Figure 51: Pipe and instrumentation diagram and construction plan based on the SUBFLOW facility: (a) Test section, (b) hot water loop, and (c) cooling heat exchanger for the main loop.

The test section housing, pins and wires are all made of transparent PMMA for optical measurements. The hot water flow can be individually adjusted inside each pin, and the heat transfer distribution is measured from the temperature distribution at the outlet. The measurement section of the wire mesh sensor was sophisticatedly designed with pin couplings that allows the wire penetration and maintain leak tightness in each flow path.

During the course of this project, it has been decided not to proceed with the construction of the wire-wrapped bundle. This decision was influenced by several factors. A review of recent literature on wire-wrapped fuel bundles highlighted a shift in research interest towards investigating pin failure mechanisms and dynamics, suggesting that investing in a large-scale bundle may not be economically efficient. Additionally, insights from a single-wire separate effect facility and simulation results conducted within the group indicate that focusing on local temperature effects in a small-scale setup could yield more valuable outcomes. An additional, unavoidable factor was the delay in securing laboratory space for the facility construction, as significant infrastructure changes at PSI in recent years have introduced substantial delays for infrastructure-related requests. Together, these factors have contributed to the decision to redirect resources toward smaller-scale, targeted studies that align better with current research priorities. In collaboration with Westinghouse, the issue of potential fuel pin cascade failures in LRF was identified as a highly important safety topic for which experimental investigations are necessary. The corresponding investigations are reported in chapter 4.

4 Pin failure cascade in LFRs

Fuel pin cladding integrity is crucial to reactor safety, as the cladding is the primary barrier between nuclear fuel and coolant. Critical failure mechanisms for LMFR fuel identified by Van Erp et al. (1972) include excessive thermal gradients, which can lead to cladding overheating through mechanisms such as thermal blanketing by gas accumulation, and mechanical stresses from shockwaves induced by neighbouring pin failure. These stresses can exceed the cladding's structure limits. Fuel pin rupture can result in either slow fission gas release (over 250 ms), potentially causing overheating to critical failure temperatures of 850–900°C, or fast release (under 100 ms), which presents a lower overheating risk. Recent analytical models by Epstein et al. (2023) explored fuel pin failure cascades in LFRs, validated against 1970s experiments on sodium-cooled fast reactors by Van Erp et al. (1972). While the model aligns with historical data, validation with only a single metal coolant remains a limitation, highlighting the need for new high-fidelity experimental data. The experimental work reported in the present chapter aims at filling this gap, providing data to enhance understanding of failure mechanisms and how to prevent overheating, mechanical degradation, and cascading fuel pins failures, all essential for reactor safety.

4.1 Experimental Facility:

An experimental facility of a single LMFR subchannel was designed and built with the goal of investigating whether the fission gases ejected by a failed pin can engulf neighbouring pins, causing deterioration of heat transfer and consequent cascade failure of the neighbouring pins. The experimental facility has been designed such that the momentum of the fission gas jet can be controlled and a visualization can be made of the liquid metal flow and gas bubble around the neighbouring pin.

The experimental facility consists of four sub-systems:

- Command-and-Control System: a Raspberry Pi 4B equipped with a custom header shield to measure pressure in the injection line during gas injection and control all valves throughout the experiment.
- Gas Injection System: a setup of valves, pressure reducers, and dosing tanks designed to inject an equivalent gas volume to that found in a full-scale fuel pin.
- Test Section: a single subchannel of a hexagonal fuel assembly with a transparent window, replicating the geometric conditions within a subchannel and featuring a gas injection orifice of 1.5 mm in diameter.
- High-Speed Camera: a LaVision HighSpeedStar camera with 16GB RAM, capable of capturing up to 500,000 frames per second, used to image the fuel pin wall.

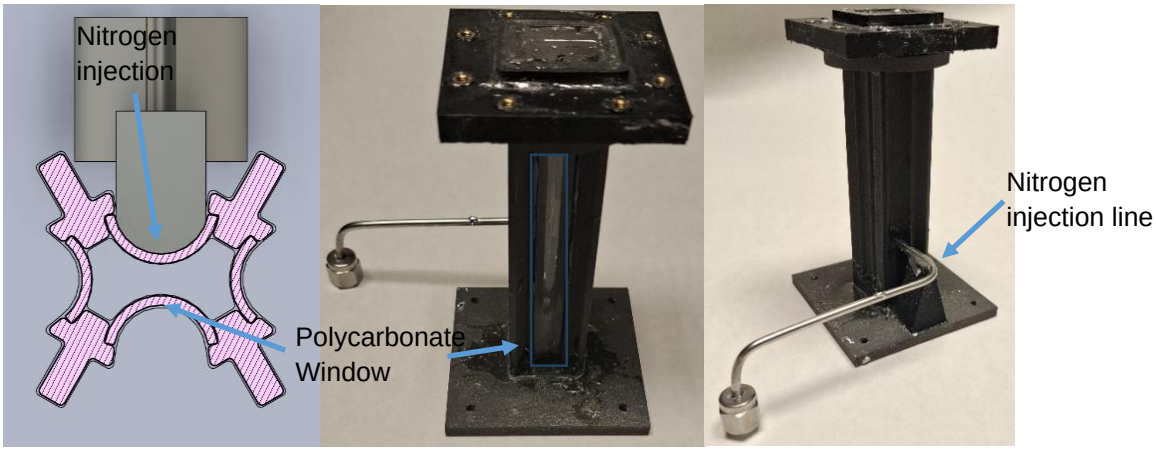

Figure 52: Experimental test-sections from different angles: (a) cross-section render from the top (b) from the front (c) from the back side

Figure 52 shows the test section used to visualize bubble impingement between fuel pins. This test section represents a single subchannel within a hexagonal fuel lattice and includes an optically transparent polycarbonate wall to observe bubble behaviour on the wall adjacent to the gas injection point. This setup is essential for assessing potential overheating of an adjacent fuel pin due to coolant absence and the presence of a thermally insulating gas bubble.

To conduct these experiments, fluid dynamic scaling was applied to substitute liquid lead with Galinstan (a gallium, indium, and tin alloy) which is liquid at room temperature, and to replace the mixture of fission gases with nitrogen. This approach allowed experiments to be performed at room temperature with precise control of initial and boundary conditions, without significantly impacting outcomes. High-speed imaging provides high-fidelity, 2D visualization of bubble formation on the adjacent fuel pin wall, with high temporal resolution (up to 500,000 frames per second) and excellent spatial resolution of the phenomenon.

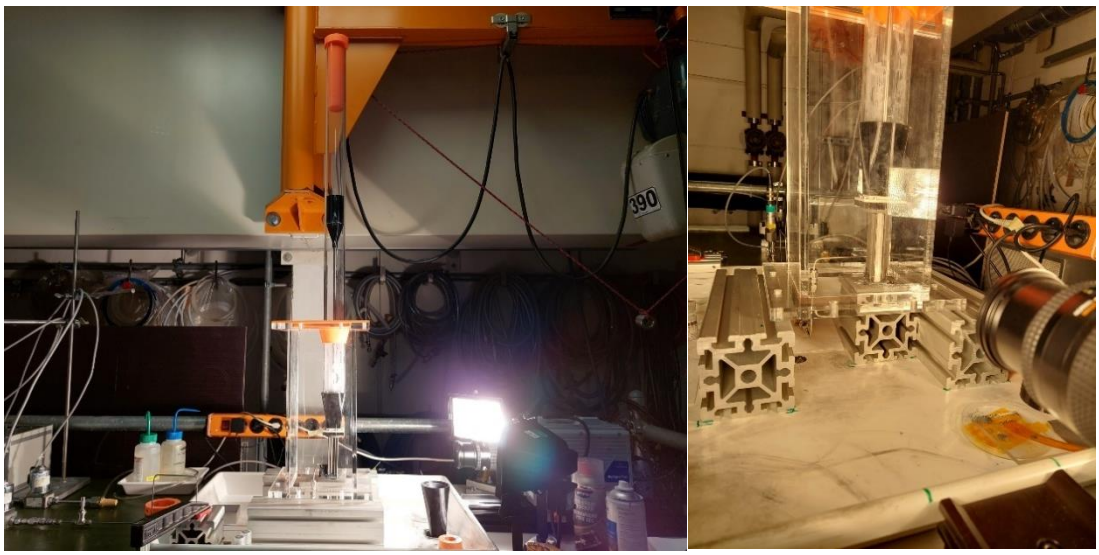

Figure 53: Experimental facility during operation: (a) Sideways view (b) Point of view of the high-speed camera

4.2 Results:

The experimental results can be subdivided into two main parts: The results of the pressure measurements and the high-speed imaging results.

4.2.1 Pressure measurements:

Epstein et al. (2023) provides an initial depressurization model of the failed fuel pin for both choked and unchoked cases, predicting the transition point between choked and unchoked flow. This model served as the initial framework for evaluating the transition point validity in the Galinstan/nitrogen pairing used here. To determine the transition point in the experimental data, an exponential fit was applied to all pressure measurements above the expected transition threshold. The point at which the experimental data began diverging from the fit was identified as the transition point. The model's prediction for the choked-to-unchoked transition closely matched the experimental data, as illustrated in Figure 54. Additionally, the model offers a correlation between the initial pressure and the fitted intercept, which also showed strong agreement with the experimental results. These findings suggest that the model accurately represents the conditions and setup in this study.

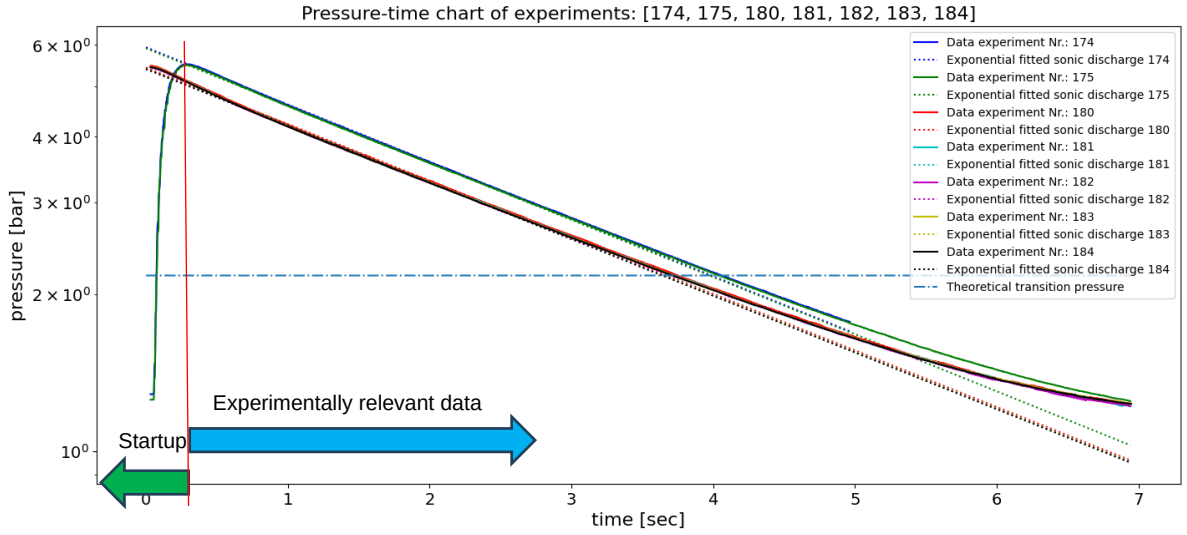

Figure 54: Experimentally measured depressurization over time

4.2.2 High-speed imaging

High-speed imaging have revealed a persistent dry spot on the fuel pin neighboring the "damaged pin" wall during the gas release, where no Galinstan adhered for over 66ms (see Figure 55). Given that the time required for a single fuel pin to overheat is approximately 250ms (Chawla and Hoglund, 1971), this dry spot poses a potential risk for cascade failure.

Across all experiments, some degree of sub-channel clearance was observed. However, at the injection site, Galinstan consistently sprayed the opposing wall, particularly just above the failure site, while less Galinstan impacted the wall directly opposite the injection site. This suggests that in the event of fuel failure, the gas blanketing on the adjacent fuel pin would likely occur slightly above the last failure point rather than directly across from it.

Two hypotheses are proposed regarding the clearing behavior observed in these experiments:

- **Counter-Current Flow Limitation (CCFL)**: due to the test section geometry and size, the injected gas volume may be too large and too energetic, causing CCFL. This would result in the formation of a single large bubble, effectively clearing the sub-channel. This behavior suggests

that the current channel dimensions may be insufficient for the gas volumes and bubble sizes involved.

- **Bubble Expansion Constraint**: The bubble may grow around the adjacent fuel pin but could be limited in lateral growth by the test section's geometry, leading to vertical expansion instead.

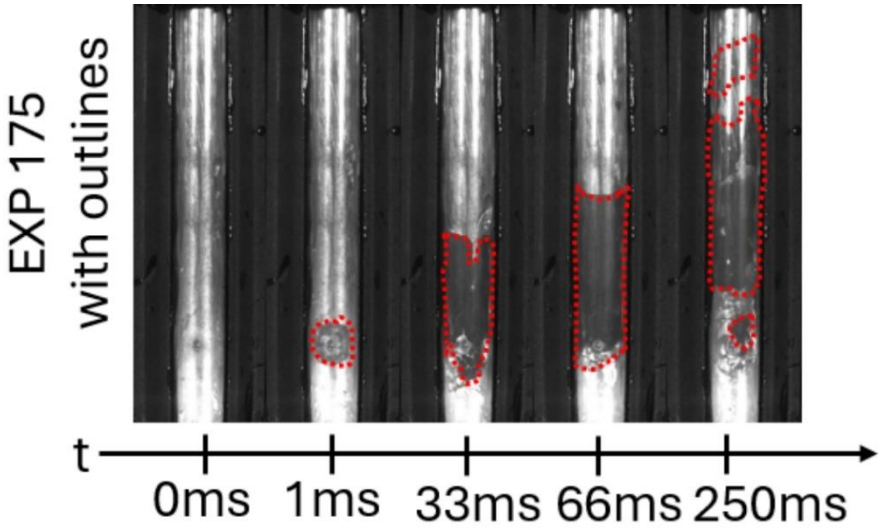

Figure 55: Highspeed imaging results from experiment 175 with bubble outlines

Further investigation of these hypotheses can be achieved with a follow-up experiment using multiple pins and a larger experimental volume.

4.3 Future work

The following topics or focus areas are being considered as potential future steps for this project:

- Scaling the test section to include additional sub-channels and assess the blanketing effect on neighboring pins: the facility will be expanded to accommodate seven pins in a hexagonal lattice arrangement, enabling full 3D bubble expansion beyond a single fuel pin subchannel.
- Implementing a conductivity-based bubble measurement system: This newly developed system enables high-speed observation of pin blanketing by measuring the gas layer in physical contact with the fuel pin surface.

Figure 56. shows renderings of the facility's CAD model (left) alongside a fully designed and assembled high-resolution 2D conductivity-based measurement system (right and bottom).

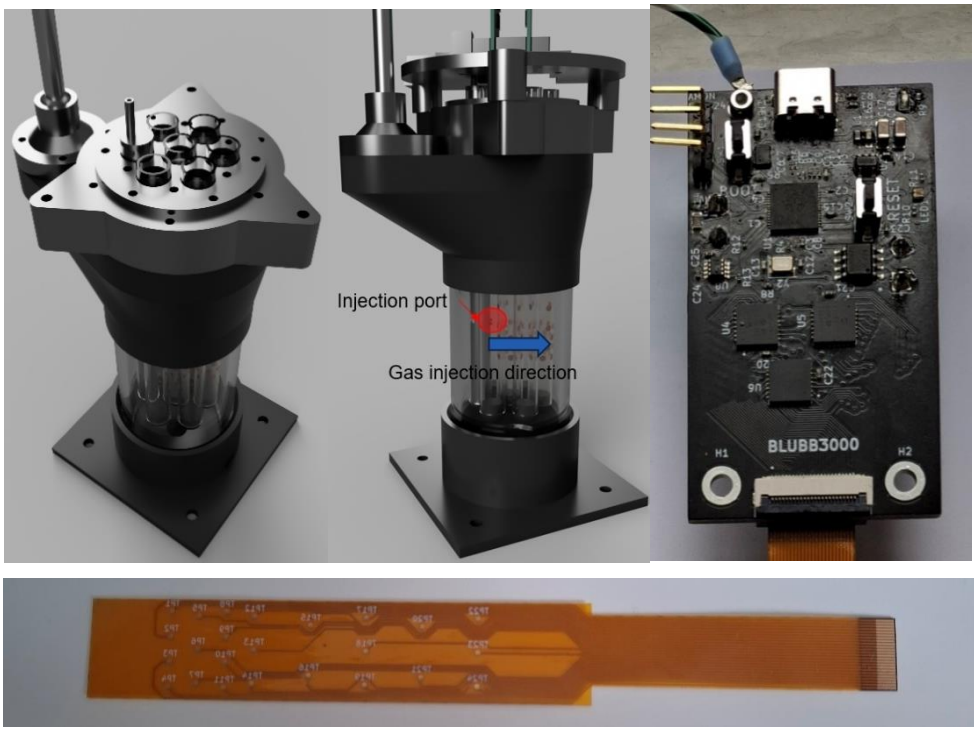

Figure 56: Next generation test-section: (a) new test-section with 7 pins (b) new test-section sideview (c) custom conductivity sensor readout system (d) first verification conductivity probe (flexible printed circuit board)

5 Conclusions

- An analytical model, based on the UNIFAC model and local composition theory, was developed and validated to accurately predicts refractive indices of mixtures. The model has been successfully applied to other properties as well such as molar volume, suggesting its value for predicting properties of complex liquid mixtures, especially when experimental data is limited. The developed analytical model can be used to systematically identified set of fluids for RIM techniques required to perform high-resolution optical measurements of liquid flows in the presence of density differences.
- An experimental facility, the MiniDestrojer, was subsequently designed and built to measure buoyant jets in uniform and stratified environments. The RIM technique has been used to allow the deployment of advanced measurement techniques, such as PIV and PLIF, enabling high-resolution analysis of complex flow structures and density gradients, which are crucial for validation of CFD models applied to stratification and buoyant flows. The RIM technique was successfully applied to study jet instabilities at various conditions. Detailed visualization of jet collapses and mixing processes were obtained. The RIM approach proved effective in analyzing liquid solutions with significant density differences, expanding the scope of quantitative studies of buoyant jets.
- An experimental facility was designed and built to investigate the occurrence of hot spots on the fuel cladding of LMFR due to the presence of a wire-wrap, typically used to prevent contact between neighboring fuel pins. High resolution measurements of the temperature behind the wire-wrap were carried out using an infrared camera. Based on dimensional parameters (Biot number), the conditions at which hot spots can occur were identified. It was also found that the geometry of the wire-wrap plays a strong role in the occurrence of cladding hot spots. Our fundings suggest that minimizing the contact area of the wire and improving fluid access beneath the wire helps mitigating the occurrence of hot spots. CFD models were then validated based on the measured experimental data and then use to predict hot spots at SFR prototypical conditions. The experimental and CFD data were then used to derive a correlation for hot spots intensity as function of relevant non-dimensionless numbers.
- For the fuel pin failure, the study demonstrated that alternative coolant-gas combinations can replicate real operating conditions, simplifying experiments. Experimental results confirmed the accuracy of Epstein et al.'s (2023) model for mass flow predictions in the sonic regime and transition pressures in subsonic flows. The sonic regime was identified as the longest phase during blowdown, making it essential in fuel pin failure modeling. Additionally, it was found that the jetting phase poses the greatest risk to adjacent fuel pins due to prolonged exposure. High-speed imaging revealed bubble growth initially localized to a single spot, with potential to surround adjacent fuel pins, indicating possible inter-pin failure propagation.

6 National and international cooperation

Within the present project, we have established a collaboration with a US research team working on the Integrated Research Project titled "Center of Excellence for Thermal-Fluids Applications in Nuclear Energy: Establishing the knowledgebase for thermal-hydraulic multiscale simulation to accelerate the deployment of advanced reactors", funded by the US Department of Energy. The US team consists of several US universities and national laboratories. The collaboration will allow Switzerland access to additional experimental data and computational results, which are not yet available in the open literature. The collaboration also provides our students and postdocs with valuable scientific exchanges on the research topic object of the present project. In addition, we have established a collaboration with Westinghouse on the topic of fuel pins cascade failure in LFRs.

7 Publications

V. Valori, V. Petrov, A. Manera, “High-fidelity experiments of turbulent buoyant jets from simultaneous Particle Image Velocimetry and Laser Induced Fluorescence”, submitted for publication in Proc. of 20th International Topical Meeting on Nuclear Reactor Thermal Hydraulics (NURETH-20), August 20–25, Washington, D.C., USA, 2023.

V. Valori, S. Qin, V. Petrov, A. Manera, “High-fidelity velocity and concentration measurements of turbulent buoyant jets”, Nuclear Technology, 2024, DOI: 10.1080/00295450.2024.2355406.

S. Nichenko, V. Petrov, A. Manera, “A Group Contribution Approach to Predicting Refractive Index and Molar Volume of Multicomponent Systems”, to be submitted (international journal).

A. Monney, V. Petrov, A. Manera, “Pin failure cascade in LFRs”, submitted for publication in Proc. of 21th International Topical Meeting on Nuclear Reactor Thermal Hydraulics (NURETH-21), August 31–September 5, Busan, South Korea, 2025.

Taehwan Ahn, Wilhelm-Martin Bissels, Victor Petrov, and Annalisa Manera, “Preliminary Experiment on Local Hot Spots in Liquid Metal Cooled Wire-wrapped Pin Bundles,” Proc. Advances in Thermal Hydraulics (ATH 2024), Orlando, FL, USA, November 17-21, (2024).

Taehwan Ahn, Wilhelm-Martin Bissels, Victor Petrov, and Annalisa Manera, “Local hot spots of the wire-wrapped pin bundle in liquid metal cooled reactors,” Proc. NURETH-21, Busan, South Korea, August 31- September 5, (2025).

Taehwan Ahn, Wilhelm-Martin Bissels, Victor Petrov, and Annalisa Manera, “Experiment on Local Hot Spots in Liquid Metal Cooled Wire-wrapped Pin Bundles,” in preparation to be submitted (international journal)

8 References

Burridge, H.C., Hunt, G.R., (2012). “The rise heights of low-and high-Froude number turbulent axisymmetric fountains”, Journal of Fluid Mechanics 691, 392–416, https://doi.org/10.1017/jfm.2011.480

Burridge, H.C., Hunt, G.R., (2016). “Entrainment by turbulent fountains”, Journal of Fluid Mechanics 790, 407–418, https://doi.org/10.1017/jfm.2016.16.

Chawla, T.C., Hoglund, B.M., (1971). “A Study of Coolant Transients During a Rapid Fission Gas Release in a Fast Reactor Subassembly”, Nuclear Science and Engineering 44.3, pp. 320–344. ISSN: 00295639. DOI: 10.13182/NSE71- A20165, www.tandfonline.com/doi/abs/10.13182/NSE71-A20165.

Clément, S.A., Guillemain, A., McCleney, A.B., Bardet, P.M., (2018). “Options for refractive index and viscosity matching to study variable density flows”, Exp. Fluids 59, 32. https://doi.org/10.1007/s00348-018-2496-1.

Collingham, R.E., Thorne, W.L., McCormack, J.D., (1971). “217-pin wire-wrapped bundle coolant mixing tests,” HEDL-TME--71-146.

Epstein, M. et al., (2023). “Models for fuel ejection from a failed annular fuel pin in a lead cooled fast reactor: Fuel/coolant interaction and fission gas/fuel jet impingement heating implications”, Annals of Nuclear Energy 181. ISSN: 18732100. DOI: 10.1016/j.anucene.2022.109499.

Fontana, M.H., MacPherson, R., Gnadt, P., Parsly, L.F., Wantland, J.L., (1973). “Temperature Distribution in a 19-Rod Simulated LMFBR Fuel Assembly in a Hexagonal Duct (Fuel Failure Mockup Bundle 2A) — Record of Experimental Data”, ORNL-TM-4113.

Fredenslund, A., Jones, R.L., Prausnitz, J.M., (1975). “Group-contribution estimation of activity coefficients in nonideal liquid mixtures”, AIChE J. 21, 1086–1099, doi.org/10.1002/aic.690210607.

Fricano, J.W., Baglietto, E., (2014). “A quantitative CFD benchmark for Sodium Fast Reactor fuel assembly modeling”, Annals of Nuclear Energy 64, pp. 32 – 42.

Geddis, P., Wu, L., McDonald, A., Chen, S., Clements, B., (2020). “Effect of static liquid Galinstan on common metals and non-metals at temperatures up to 200°C”, Canadian Journal of Chemistry. https://doi.org/10.1139/cjc-2020-0227.

Hrycak, P., Jachna, S., Lee, D., (1974). “A study of characteristics of developing, incompressible, axi-symmetric jets”, Letters in Heat and Mass Transfer, vol. 1, pp. 63-72.

IAEA, (2012). “Liquid Metal Coolants for Fast Reactors Cooled By Sodium, Lead, and Lead-Bismuth Eutectic”, Vienna, Austria: IAEA Nuclear Energy Series No. NP-T-1.6, https://www-pub.iaea.org/MTCD/publications/PDF/P1567_web.pdf.

Jain, M., Attarde, D., Gupta, S.K. (2017). “Estimation of unknown UNIFAC interaction parameters between thiophene and olefin, and thiol and olefin functional groups”, Fluid Phase Equilibria 442, 81–86, https://doi.org/10.1016/j.fluid.2017.03.019.

Kang, J.W., Diky, V., Chirico, R.D., Magee, J.W., Muzny, C.D., Abdulagatov, I., Kazakov, A.F., Frenkel, M., (2011). “A new method for evaluation of UNIFAC interaction parameters”, Fluid Phase Equilibria 309, 68–75. https://doi.org/10.1016/j.fluid.2011.07.001.

Krohn, B., Manera, A., Petrov, V., (2018). "A novel method to create high density stratification with matching refractive index for optical flow investigations." Experiments in Fluids, p. 59-66.

List, E. J., (1982). "Mechanics of Turbulent Buoyant Jets and Plumes," in HMT: the Science & Applications of Heat and Mass Transfer. Reports, Reviews & Computer Programs, Pergamon, pp. 1-68.

Nathan, G. J., Mi, J., Alwahabi, Z. T., Newbold, G. J. R., Nobes, D. S., (2006). “Impacts of a jet’s exit flow pattern on mixing and combustion performance”, Progress in Energy and Combustion Science, vol. 32, pp. 496-538, 2006.

Paladino, D., Andreani, M., Zboray, R., Dreier, J., (2012). “Toward a CFD-grade database addressing LWR containment phenomena”, Nuclear Engineering and Design, vol. 253, pp. 331-342.

Philippe, P., Raufaste, C., Kurowski, P.,Petitjeans, P., (2005). “Penetration of a negatively buoyant jet in a miscible liquid”, Physics of Fluids 17, 1–10, https: //doi.org/10.1063/1.1907735.

Qin, S., Krohn, B., Downing, J., Petrov, V., Manera, A. (2018). "High-Resolution Velocity Field Measurements of Turbulent Round Free Jets in Uniform Environments." Nuclear Technology.

Rodi, W. (1975). “A new method of analysing hot-wires signals in highly turbulent flow, and its evaluation in a round jet”, DISA Info.

Shashikant, M. A., et al., (2013). LES and RANS simulations of the ANL MAX experiment for various inlet boundary conditions. Argonne National Laboratory, MCS/ANL-TM-337.

Singh, R.P., Pathanjali, G.A., (1987). “UNIFAC interaction parameters for excess enthalpies of mixing”, Thermochim. Acta 111, 267–274, https://doi.org/10.1016/0040-6031(87)88053-X.

Valori, V., Qin, S., Petrov, V., Manera, A. (2024), “High-fidelity velocity and concentration measurements of turbulent buoyant jets”, https://doi.org/10.48550/ARXIV.2402.16610.

Van Erp, J.B., Chawla, T.C., Wilson, R.E., (1972). “Potential Fuel Failure Propagation Due to Fission-Gas Release in LMFBR Subassemblies”, ASME 72.14.

Williamson, N., Srinarayana, N., Armfield, S.W., Mcbain, G.D., Lin,W., (2008). “Low-reynolds-number fountain behaviour”, Journal of Fluid Mechanics 608, 297–317, doi.org/ 10.1017/S0022112008002310.

Wygnanski, I., Fiedler, H., (1969). “Some measurements in the self-preserving jet”, Journal of Fluid Mechanics, vol. 38, pp. 577-612.

Zhang, W., He, Z., Jiang, H., (2017). “Scaling for turbulent viscosity of buoyant plumes in stratified fluids: PIV measurement with implications for submarine hydrothermal plume turbulence”, Deep Sea Res. Part Oceanogr. Res. Pap. 129, 89–98. https://doi.org/10.1016/j.dsr.2017.10.006.

First page image compiled from www.nrc.gov/docs/ML1915/ML19150A397.pdf and www.mhi.co.jp